J. Fluid Mech. (2007), *vol.* 571, *pp.* 1–32. © 2007 Cambridge University Press
doi:10.1017/S002211200600320X Printed in the United Kingdom

Rheology of surface granular flows

By ASHISH V. ORPE AND D. V. KHAKHAR

Department of Chemical Engineering, Indian Institute of Technology, Bombay, Powai, Mumbai 400076, India

(Received 14 June 2005 and in revised form 14 June 2006)

Surface granular flow, comprising granular material flowing on the surface of a heap of the same material, occurs in several industrial and natural systems. The rheology of such a flow was investigated by means of measurements of velocity and number-density profiles in a quasi-two-dimensional rotating cylinder, half-filled with a model granular material – monosize spherical stainless-steel particles. The measurements were made at the centre of the cylinder, where the flow is fully developed, using streakline photography and image analysis. The stress profile was computed from the number-density profile using a force balance which takes into account wall friction. Mean-velocity and root-mean-square (r.m.s.)-velocity profiles are reported for different particle sizes and cylinder rotation speeds. The profiles for the mean velocity superimpose when distance is scaled by the particle diameter d and velocity by a characteristic shear rate $\dot{\gamma}_C = [g \sin(\beta_m - \beta_s)/d \cos \beta_s]^{1/2}$ and the particle diameter, where β_m is the maximum dynamic angle of repose and β_s is the static angle of repose. The maximum dynamic angle of repose is found to vary with the local flow rate. The scaling is also found to work for the r.m.s. velocity profiles. The mean velocity is found to decay exponentially with depth in the bed, with decay length $\lambda = 1.1d$. The r.m.s. velocity shows similar behaviour but with $\lambda = 1.7d$. The r.m.s. velocity profile shows two regimes: near the free surface the r.m.s. velocity is nearly constant and below a transition point it decays linearly with depth. The shear rate, obtained by numerical differentiation of the velocity profile, is not constant anywhere in the layer and has a maximum which occurs at the same depth as the transition in the r.m.s. velocity profile. Above the transition point the velocity distributions are Gaussian and below the transition point the velocity distributions gradually approach a Poisson distribution. The shear stress increases roughly linearly with depth. The variation in the apparent viscosity η with r.m.s. velocity u shows a relatively sharp transition at the shear-rate maximum, and in the region below this point the apparent viscosity $\eta \sim u^{-1.5}$. The measurements indicate that the flow comprises two layers: an upper low-viscosity layer with a nearly constant r.m.s. velocity and a lower layer of increasing viscosity with a decreasing r.m.s. velocity. The thickness of the upper layer depends on the local flow rate and is independent of particle diameter while the reverse is found to hold for the lower-layer thickness. The experimental data is compared with the predictions of three models for granular flow.

1. Introduction

Surface flows of granular materials comprise a shallow layer of particles flowing on a fixed bed (heap) of the same particles. Such flows are encountered in several industrial operations as well as in nature. Industrial examples appear in the processing of material in systems such as rotary kilns (Peray 1986) and tumbling mixers (Perry &

https://doi.org/10.1017/S002211200600320X Published online by Cambridge University Press

Green 1997), in the formation of heaps for storage and in the feeding and discharge of hoppers and silos (Nedderman 1992). Natural examples are the formation of sand dunes (Andreotti, Claudin & Douady 2002*a*, *b*; Wang & Zheng 2004), avalanches (Hutter, Koch & Savage 1995; Hutter 1997) and the transport of sediment in rivers (Bounhoure, Brunet & Merlen 2002).

Surface granular flows have one unique feature that differentiates them from other granular shear flows. The 'boundary' between the flowing particles and the fixed bed is determined by the flow itself. A consequence is that interchange of particles between the flowing layer and the bed is possible, and the local surface angle and the local layer thickness vary with the local flow. Although it is reasonable to picture the flow in terms of two distinct regions (a flowing layer and a fixed bed) separated by a sharp interface, in fact the boundary is diffuse and the flow decays to zero exponentially with depth. Thus a homogeneous and responsive boundary exists at the base of the flow which is quite different in qualitative terms from a flow on an inclined rough surface. Several studies have been carried out to understand the physics of surface granular flows and a review of the previous work is given below.

Rotating cylinders and heaps have been the primary systems used for the experimental study of surface granular flows. In both systems, the major component of the velocity is parallel to the surface and the velocity profile is found to be broadly linear across the layer (Nakagawa *et al.* 1993; Rajchenbach, Clement & Duran 1995; Bonamy, Daviaud & Laurent 2002*a*; Jain, Ottino & Lueptow 2002; Longo & Lamberti 2002; Taberlet *et al.* 2003; Orpe & Khakhar 2004). Komatsu *et al.* (2001) showed the decay of the velocity to be exponential with depth and this has been confirmed in several subsequent studies (Jain *et al.* 2002; Bonamy *et al.* 2002*a*; Longo & Lamberti 2002; Taberlet *et al.* 2003; Orpe & Khakhar 2004). The flux in the region of exponential decay is relatively small and there has been a focus on the shear rate corresponding to the linear part. Some studies show that the shear rate is nearly constant and independent of the local mass-flow rate, particularly for low mass-flow rates and near-two-dimensional systems (Rajchenbach *et al.* 1995; Khakhar *et al.* 2001*a*; Bonamy *et al.* 2002*a*). In other cases the shear rate is found to increase with flow rate (Orpe & Khakhar 2001; Jain *et al.* 2002). The bulk density is nearly constant across the layer and approaches close packing (Rajchenbach *et al.* 1995; Bonamy *et al.* 2002*a*; Jain *et al.* 2002; Orpe & Khakhar 2004), indicating the highly dissipative nature of the flow.

The surface angle β is found to increase with mass-flow rate in the layer (Khakhar *et al.* 2001*a*; Orpe & Khakhar 2001); however, in these and similar studies the measurements were made near a wall. Recently Taberlet *et al.* (2003) showed a systematic effect of the wall on the surface angle. They found that the measured increase in angle with flow rate in heap-flow experiments could be accounted for by considering the effect of wall friction in a force balance. The analysis yields $\tan\beta = \mu_i + \mu_w\delta/b$, where δ is the layer thickness, b is the gap width, μ_i is the effective coefficient of friction and μ_w is the coefficient of friction between the particles and wall. Thus for sufficiently wide gaps ($\delta/b \gg 1$) a constant surface angle should be obtained. This was indeed observed by Jop, Forterre & Pouliquen (2005) in a systematic experimental study of the effect of gap width on heap flow. They found that the gap width between the side walls also affects the mean velocity and the depth of the flowing layer. As the gap width is increased the surface angle decreases, the mean velocity decreases and the depth of the flowing layer increases. The rate of increase in surface angle with flow rate reduces with the gap width, and at the highest gap width considered (570 particle diameters) the surface angle is nearly independent

https://doi.org/10.1017/S002211200600320X Published online by Cambridge University Press

of the flow rate. Down-channel velocity profiles measured at the free surface indicate that the range of the 'wall effect' extends to a greater distance from each wall with increasing gap width, even when the lengths are scaled by the gap width. This, however, may be a reflection of the fact that the flow rate varies significantly across the gap. Courrech-DuPont *et al.* (2005) measured the instantaneous velocity profiles during an avalanche in a rotating cylinder. The profiles obtained at different times at the centre of the cylinder were self-similar and had an exponential dependence on the depth. The linear part of the profile, found for steady flows, was not seen. Jain *et al.* (2002) reported measurements of the granular temperature, which is an important input in some models for the flow. The qualitative features of the flow remain unchanged even when the particles are completely immersed in a liquid (Jain, Ottino & Lueptow 2004). The flow in a two-dimensional rotating cylinder and its rheology were studied by Renouf *et al.* (2005) by means of contact-dynamics simulations.

The simplest models for surface flow comprise a depth-averaged mass-balance equation in the flowing layer with a phenomenological equation for the flux from the bed to the layer that is assumed to be determined by the local angle of the surface (Bouchaud *et al.* 1994; Mehta 1994; Boutreux & de Gennes 1996; Boutreux, Raphaël & de Gennes 1998). More detailed depth-averaged continuum models also yield similar equations (Khakhar *et al.* 1997; Douady, Andreotti & Daerr 1999; Khakhar *et al.* 2001*a*) and agree well with the experimental results (Khakhar *et al.* 2001*a*, *b*). The main difference in these models is the stress constitutive equation used. One approach is to assume the shear rate to be a known constant; this eliminates the need for the stress constitutive equation (Douady *et al.* 1999; Makse 1999). Rajchenbach (2003) gave a physical justification for a constant shear rate based on the assumption that a single collision entirely dissipates the momentum of both colliding particles. This yields an estimate for the shear rate as $\dot{\gamma} \sim (g \sin\beta/d)^{1/2}$, where β is the local surface angle of flow, d is the particle diameter and g is the acceleration due to gravity. Such an approach gives good predictions of the experimental results for rotating-cylinder flow at low rotational speeds (Makse 1999). A phenomenological equation for the stress based on frictional and collisional contributions (Khakhar *et al.* 1997; Orpe & Khakhar 2001; Khakhar *et al.* 2001*a*) gives a somewhat different expression for the shear rate,

$$\dot{\gamma} = \left[\frac{g \sin(\beta_m - \beta_s)}{cd \cos\beta_s}\right]^{1/2}, \tag{1.1}$$

where β_m is the maximum dynamic angle of repose, β_s is the static angle of repose and c is a constant. In the context of the model, β_m is the free surface angle for a steady fully developed flow with no interchange and corresponds to the neutral angle of the BRdG model (Boutreux *et al.* 1998). As we shall see below, β_m is not a material property and varies with the local flow rate. The continuum model based on the phenomenological stress equation gives good predictions of the layer-thickness profile and the shear rate for both heap flows (Khakhar *et al.* 2001*a*) and rotating cylinder flows (Orpe & Khakhar 2001). The model predicts a nearly constant shear rate at low flow rates (Khakhar *et al.* 2001 *b*). We note that (1.1) relates to the analysis of Quartier *et al.* (2000) for the motion of a single particle down a bumpy inclined plane. If the effective acceleration proposed by Quartier *et al.* (2000) is considered together with the particle diameter as a length scale, a scaling analysis yields an expression similar to (1.1) for the shear rate.

https://doi.org/10.1017/S002211200600320X Published online by Cambridge University Press

More detailed rheological models for the dense granular flow typical of surface flows have also been proposed, based on different approaches. Savage (1998) developed a kinetic theory based on strain-rate fluctuations that are related to the granular temperature. The resulting governing equations contain a viscosity term that shows a decrease with an increase in the granular temperature, similar to that for a liquid. Bocquet *et al.* (2001) modified granular kinetic-theory equations to give a sharper increase in the granular viscosity with the solid-volume fraction. The model gave good predictions of the velocity profile in a Couette flow. A two-phase solid–liquid model was proposed by Aranson & Tsimring (2002), the fraction of the solid phase present locally being determined by an order parameter. This model is described in more detail in § 3.4 and its predictions are compared with the experimental results. Josserand, Lagree & Lhuillier (2004) proposed a continuum model based on stress constitutive equations which depend on the local volume fraction. The model gives a reasonable qualitative description of surface flows. Dense granular flows have also been described by Cosserat-type constitutive models in which local couple-stresses due to particle rotations are taken into account. A Cosserat model was proposed by Mohan, Nott & Rao (2002) and predictions of the model for the velocity profile were shown to be in good agreement with measurements in a vertical channel flow and in a dense Couette flow. Recently Pouliquen and coworkers (MiDi 2004; Jop *et al.* 2005) proposed that the local shear stress in a granular flow may be expressed in terms of a shear-rate ($\dot{\gamma}$) dependent effective friction coefficient of the following form:

$$\mu = \mu_s + \frac{\mu_2 - \mu_s}{I_0/I + 1}, \tag{1.2}$$

where $I = d\dot{\gamma}(P/\rho_p)^{1/2}$ is the dimensionless shear rate with ρ_p the particle density and P the granular pressure; μ_s, μ_2 and I_0 are model parameters. The model is found to work well for flow on a rough inclined plane and for heap flow (Jop *et al.* 2005). We shall compare our experimental results with this model as well. Numerical simulations in two-dimensions (Renouf *et al.* 2005; DaCruz *et al.* 2005) have also shown I to be a useful parameter for describing granular rheology.

All the models discussed above are based on a local stress constitutive equation. The high density of the flow results in multiparticle contacts and thus there is a distinct possibility of non-local transfer of stresses. Several theories have explored such ideas. Pouliquen, Forterre & Le Dizes (2001) considered stress transfer by fluctuations in the bed. The fluctuations decay with distance from their point of origin. The model gives good predictions of data for dense flows in vertical and inclined channels. Mills, Loggia & Tixier (1999) and Bonamy & Mills (2003) considered dense shear flows in which near-vertical particle chains are formed by gravity forces. The model gives good predictions of measured velocity profiles. The predictions of this model are also compared with our experimental data below.

The rheology of surface granular flows has not been experimentally explored in detail as yet and is the focus of the present work. Our objective was to carry out an experimental study and analysis of the flow and rheology of a steady fully developed surface granular flow. A quasi-two-dimensional rotating-cylinder system (gap width 5–10 particle diameters) was used and the measurements were made in the region near the cylinder axis where the flow is fully developed and steady. Experiments were carried out over a range of particle sizes and rotational speeds, and the data were analyzed by scaling and comparison with existing models. Section 2 gives the details of the experimental system and methods used. The results are discussed in § 3 and are followed by our conclusions in § 4.

https://doi.org/10.1017/S002211200600320X Published online by Cambridge University Press

Material	Diameter d (mm)	Mass m (mg)	Particle density ρ_p, (kg m^3)	Bulk density ρ_b, (kg m^3)	Young's modulus (GPa)
	1	4.2 ± 0.06		4973	
Stainless steel	2	33.5 ± 0.18	8000	4899	200
	3	112.5 ± 0.18		4725	
Brass	2	35.0 ± 0.25	8500	5205	120

TABLE 1. Geometrical and physical properties of the particles used in the experiments.

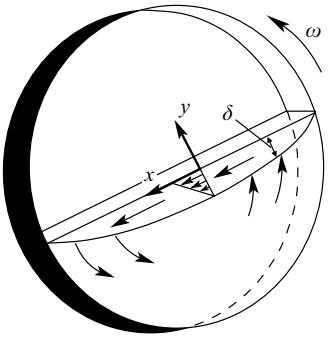


FIGURE 1. Schematic view of the flow in a rotating cylinder, comprising a surface-flowing layer of thickness $\delta(x)$ and a packed bed of particles rotating with the cylinder. The coordinate system employed in the analysis is shown.

2. Experimental details

We first describe the experimental system used for this work. The experimental method, based on digital photography, is discussed next and then a description of the technique used for analyzing the digital images follows.

2.1. *System*

The experiments were carried out in quasi-two-dimensional aluminium cylinders (length $b = 1$ or 2 cm) of radius 16 cm. The end walls were made of glass to enable visualization of the particle motion. A computer-controlled stepper motor with a sufficiently small step was used to rotate the cylinders. Stainless steel (SS) balls of three different sizes with diameters (d) 1, 2, and 3 mm were used in the experiments. A few experiments were carried out using 2 mm brass balls to investigate the effect of material characteristics. Brass is a heavier and softer material as compared to SS. The properties of all the particles used are listed in table 1. All the particles used in the experiments were accurately spherical in shape (the SS balls are the type used as ball bearings). The surfaces of all the particles were smooth and reflective; this facilitated the image-analysis method used in this work. Table 1 indicates that the bulk density is higher for the smaller particles. This is a result of the lower packing density near the walls for all the particles. Since the gap width b is the same in all cases, the fraction of particles in the wall region is smaller for the smaller particles resulting in a higher overall bulk density.

Experiments were carried out at different rotational speeds ($\omega = 2$–9 r.p.m.) such that the flow was always in the rolling regime. The typical flow pattern, comprising a surface-flowing layer of varying thickness $\delta(x)$ and the bed rotating at the angular speed of the drum, ω, is shown schematically in figure 1. The particles are heavy

https://doi.org/10.1017/S002211200600320X Published online by Cambridge University Press

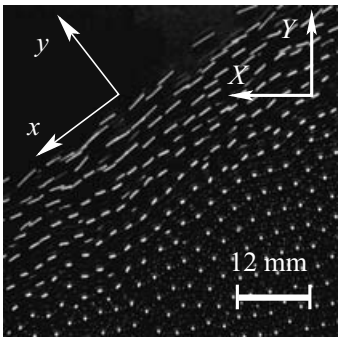


FIGURE 2. Flow of SS balls of diameter 2 mm for an angular speed ω of 3 r.p.m. Streaks correspond to the particle displacement during the time the shutter is open, $\Delta t = 1/500$ s. The coordinates x,y correspond to a y-axis along the free surface of the flowing layer, while X,Y are the coordinates in the laboratory reference frame.

enough and sufficiently conductive that static-charge effects are negligible. All the experiments were carried out with the cylinder half-full of particles (i.e. a fill fraction of 50 %).

2.2. *Experimental method*

The measurements in the flowing layer were made near the centre of the cylinder ($x = 0$, in figure 1), where the layer thickness is a maximum and the flow is nearly unidirectional and non-accelerating (the velocity is nearly invariant in the x-direction). The images were taken keeping the camera close to the face plate of the cylinder and framing a small region of the flow. The size of the recorded region was 2560×1920 pixels; one pixel corresponded to 0.016–0.03 mm, depending on the distance of the camera from the cylinder. A point source of light was directed nearly parallel to the face plate of the cylinder so as to illuminate only the front layer of the flowing particles. Owing to the high sphericity and the polished surface of the particles, a well-defined reflection is produced from each stationary particle (see figure 2, lower right corner). Each moving particle generates a streak of definite length depending on its speed and the shutter speed of the camera. Figure 2 shows a typical image with streaks of different lengths in the flowing layer. The velocity of each particle is determined from the length and orientation of the streak formed; the analysis method is explained in § 2.3. This method of velocity determination is similar to that used by Rajchenbach *et al.* (1995).

Images were taken for a range of camera shutter speeds ($1/15 - 1/1000$ s) so as to account for the varying velocity across the flowing layer. About 100 images were taken for each shutter speed with a total of 1000 images combined over different shutter speeds. Each experiment was carried out for about 500 revolutions, two images being taken per revolution. Thus the flow was sampled over a considerable time period ($\sim$ 3 h). The images were analysed to determine the velocity and number-density profiles across the layer.

2.3. *Image analysis*

The image-analysis technique involved identification of the streaks in the front layer followed by determination of the length and the orientation of each identified streak. Computer codes were written to manipulate and analyse the digital images. Details are given below.

https://doi.org/10.1017/S002211200600320X Published online by Cambridge University Press

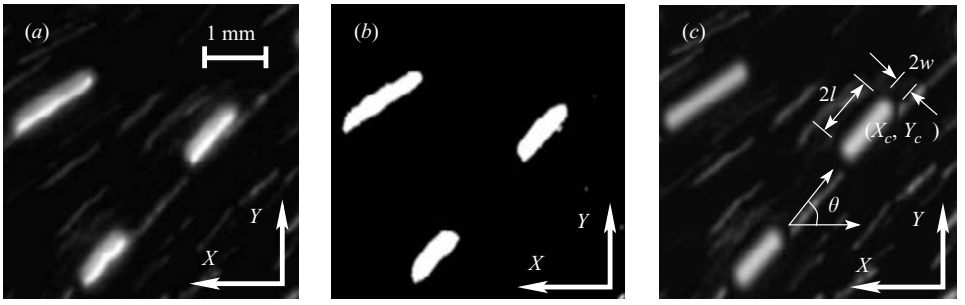


FIGURE 3. Image analysis of streaks. (*a*) Original image of the streaks. (*b*) Thresholded streaks with pixels identified in each streak. (*c*) Fitting of the function (2.1) to one streak. X, Y are the coordinates in the laboratory reference frame. (X_c, Y_c) is the position of the streak in this frame of reference. $2l$ and $2w$ are the length and width of the streak, respectively. θ is the orientation of the streak to the horizontal.

Each image is first converted to black and white by putting the intensity values of pixels greater than a certain threshold to white and the rest to black. The threshold was chosen so that the streaks from the front layer are converted to white and the streaks in the back layers, which are less illuminated, to black. All the photographs were taken with a black background so as to make the thresholding easier. The thresholded image is scanned row by row to identify clusters of contiguous white pixels. Clusters smaller than a specified size (75 pixels) are due to reflection of the light from the periphery of the particle surface and are eliminated. Clusters larger than this size are taken to be streaks. Figure 3(*a*) shows three magnified streaks in the front layer and a number of faint streaks from the back layers. Figure 3(*b*) shows the thresholded image with the faint streaks eliminated.

In the next stage of the analysis, the position, length and angle of each streak is determined by fitting a parameterized intensity function to the intensity values of the streak pixels (and an immediate neighbourhood) in the original image. An intensity function of the following form is used:

$$I_{th} = \begin{cases} C\mathrm{e}^{-\bar{y}^2/4w^2}, & |\bar{x}| \leqslant l, \quad (2.1a) \\ C\mathrm{e}^{[-\bar{y}^2-(\bar{x}-l)^2]/4w^2}, & |\bar{x}| > l, \quad (2.1b) \end{cases}$$

where $\bar{x} = (X - X_c)\cos\theta + (Y - Y_c)\sin\theta$, $\bar{y} = (Y - Y_c)\cos\theta - (X - X_c)\sin\theta$, $2l$ is the nominal length of the streak, $2w$ is the nominal width of the streak, θ is the orientation of the streak to the horizontal and C is the maximum intensity value obtained at the centroid of the streak. (X_c, Y_c) is the position of the centroid of the streak in laboratory coordinates (figure 3*c*).

Initial estimates of the position (X_c, Y_c), length $2l$, width $2w$ and orientation angle θ are first obtained for an identified streak from the thresholded image. The values are refined by minimizing the following function for each streak using Powell's method (Press *et al.* 1994):

$$f = \sum (I_{th} - I_{image})^2, \quad (2.2)$$

where I_{image} is the intensity value for a pixel in the original image at that point (figure 3*a*). The summation in (2.2) is carried out over all the pixels of the cluster corresponding to a streak, together with six layers of pixels added to the cluster. Figure 3(*c*) shows the computed intensity values plotted on the original image using the fitted parameters.

https://doi.org/10.1017/S002211200600320X Published online by Cambridge University Press

The velocity magnitude is $v = 2L/\Delta t$, where Δt is the time interval corresponding to the shutter speed set in the camera and the velocity components are calculated from the orientation angle θ; $L = L(l, w)$ is the distance moved by the particle in the time interval Δt and is obtained as a function of the streak length and width using calibration experiments described below. The position corresponding to this velocity vector is taken to be the centroid of the streak (X_c, Y_c). A similar procedure is applied for every streak identified in an image. Only streaks with lengths in the range 20–70 pixels are considered for analysis. The reason is that streaks longer than 70 pixels tend to overlap other streaks, while those shorter than 20 pixels result in an inaccurate determination of the orientation angle θ. The use of different shutter speeds gives streaks with lengths within this range at each depth in the layer. Streaks which are cut off at the edges of an image are not considered for velocity calculation.

The analysis results from all the images are combined and the coordinate positions for all the selected streaks are rotated by an angle θ_{avg}. This angle is determined by averaging the angle of orientation θ for all the streaks in the selected region of the flowing layer, and represents the orientation of the flowing layer to the horizontal. The components c_z and c_y of the instantaneous velocity parallel and perpendicular to the flow direction are determined for every streak from its orientation angle θ. The region shown in figure 2 is then divided into bins of depth equal to the particle diameter and length 20 mm parallel to the flowing layer. The profiles of the averaged parallel, v_x and v_y, and perpendicular components of velocity are then generated by averaging the instantaneous velocity components c_x, c_y over all the streaks in each bin.

In a typical measured velocity profile, the average x-velocity v_x decreases and then starts to increase with depth in the flowing layer from the free surface, because the velocity decreases and eventually becomes negative (owing to bed rotation) with decreasing y. However, our technique cannot give the direction of the velocity vector. Hence we assume all velocities below the minimum-velocity point to be negative.

The root-mean-square (r.m.s.) velocity and its components in the x- and y- directions are calculated from the instantaneous velocities using the following equations:

$$u_x = \sqrt{\overline{c_x^2} - (\overline{c_x})^2}, \tag{2.3a}$$

$$u_y = \sqrt{\overline{c_y^2} - (\overline{c_y})^2}, \tag{2.3b}$$

$$u = \sqrt{u_x^2 + u_y^2}, \tag{2.3c}$$

where the overbar indicates an average over all streaks in a bin corresponding to a particular y-coordinate. The number-density profiles are obtained from a separate set of images at a high shutter speed (1/2000 s). Such high shutter speeds ensure that streaks are short ($\leqslant 30$ pixels) and do not overlap, so that all the streaks in an image can be used for analysis. This is required to get an accurate number count. Images are analysed in the same manner as mentioned above, but only the centroid positions are noted. The number density for any y is determined by counting the number of particles in each bin. A source of inaccuracy is that particles from back layers may also be counted, which leads to an overestimate of the number densities. This is particularly the case for the low-number-density region near the free surface. Further, the measurements represent densities near the wall, which are different from those in the bulk.

https://doi.org/10.1017/S002211200600320X Published online by Cambridge University Press

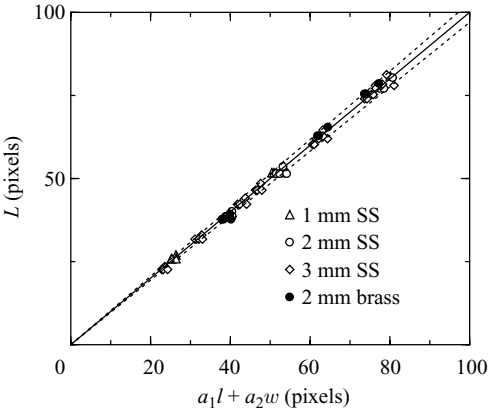


FIGURE 4. Calibration results for determining streak lengths. Variation in actual streak length L with a linear sum of the length l and width w of a streak measured by image analysis; $a_1 = 2.05$ and $a_2 = 1.86$ are the constants obtained by linear regression of the experimental data. The dotted lines represent a 3% deviation in the calculation of L.

Experiments were carried out to calibrate the analysis technique. A single particle was glued to the face plate of the cylinder on the inner side at a position close to the periphery of the cylinder. The radial position of the particle was accurately determined and from this the velocity of the particle can be obtained since the angular speed of the cylinder is known. The cylinder was rotated at different angular speeds and images of this particle are taken at different camera shutter speeds (1/30–1/500 s). The size of the recorded region and the lighting conditions were the same as those used for the measurements in the flowing layer. Further, the rotational speed of the cylinder and the shutter speeds were adjusted so as to generate streaks of three different lengths. The maximum and minimum lengths of the streaks span the range of streak lengths considered for velocity measurements in the flowing layer. The experiments were carried out for all the particles used in the experiments. The length $2l$, width $2w$, position (X_c, Y_c) and orientation θ of a single streak were determined in each case using the same analysis procedure as described earlier. The actual distance L travelled by a particle at radial distance r ($L = \omega r \Delta t$) is known from the linear velocity of the particle, ωr, and the shutter speed used, Δt. A linear relation of the following form is assumed to hold between the actual length L and the measured length l and width w of each streak:

$$L = a_1 l + a_2 w. \tag{2.4}$$

The constants a_1 and a_2 were determined by a least-squares fit to the experimental data combined for particles of different sizes and materials. The fit yielded $a_1 = 2.05$ and $a_2 = 1.86$ with a standard error of about 1.1 pixels. Figure 4 shows for comparison the measured and fitted streaks. The experimental data are well correlated by (2.4) and indicate that the actual distance travelled by a particle depends on both the length and the width parameters of the intensity function. The error in calculating L is less than 3 % (figure 4) and represents the typical error in measurements of velocities in the flowing layer.

The maximum dynamic angle of repose β_m was taken to be the angle θ_{avg} by which the data is rotated to obtain $v_y = 0$. The static angle of repose β_s was taken to be the angle of the stationary free surface when the rotation of the cylinder, operating

https://doi.org/10.1017/S002211200600320X Published online by Cambridge University Press

Material	d (mm)	ω (r.p.m.)	β_m (deg.)	β_s (deg.)	q (cm^2 s^{-1})
	1	2	25.6	16.0	26.8
	1	3	26.6	16.0	40.2
Stainless steel	2	3	29.1	20.1	
	2	6	35.7	20.1	80.4
	2	9	42.8	20.1	120.6
	3	3	26.3	18.4	
Brass	2	3	27.8	18.3	

TABLE 2. Experimentally determined values of the angles β_m and β_s and calculated volumetric flow rate per unit width q for the different cases studied.

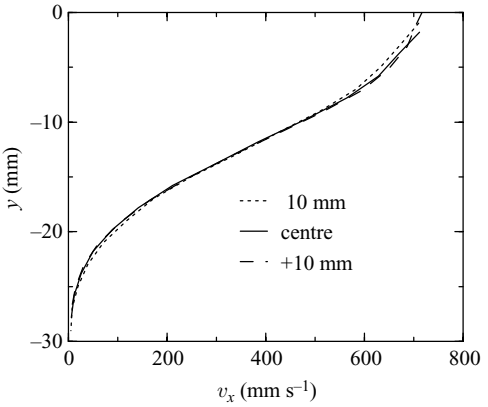


FIGURE 5. Mean velocity profiles measured at three locations along the layer, as indicated in the legend, for 2 mm particles with the cylinder rotated at 3 r.p.m.

under steady-flow conditions, stopped. The values of β_m and β_s (averaged over six images) are reported in table 2 for all the cases studied. We also checked that the flow was fully developed by measuring the velocity profile at two additional locations, one 10 mm upstream and one 10 mm downstream of the layer midpoint ($x = 0$). Figure 5 shows the profiles of the mean velocity at the three locations for one case (2 mm particles in the cylinder rotated at 3 r.p.m.). The profiles are identical within experimental error, verifying that the flow was fully developed.

3. Results and discussion

We first present the experimental results obtained for varying system parameters. Scaling and the analysis of the experimental profiles are presented next. The rheology of the flow is discussed in § 3.3. Finally, we compare our experimental velocity profiles with the predictions of the models of Bonamy & Mills (2003), Aranson & Tsimring (2002) and Pouliquen and coworkers (Jop *et al.* 2005, MiDi 2004).

3.1. *Base data*

The primary parameters varied in the experiments are the cylinder rotational speed ω and the particle diameter d, and the results presented below are in terms of these parameters. There is, however, a direct relation between the cylinder rotational speed and the local volumetric flow rate per unit gap width q. A mass balance for a half-full

https://doi.org/10.1017/S002211200600320X Published online by Cambridge University Press

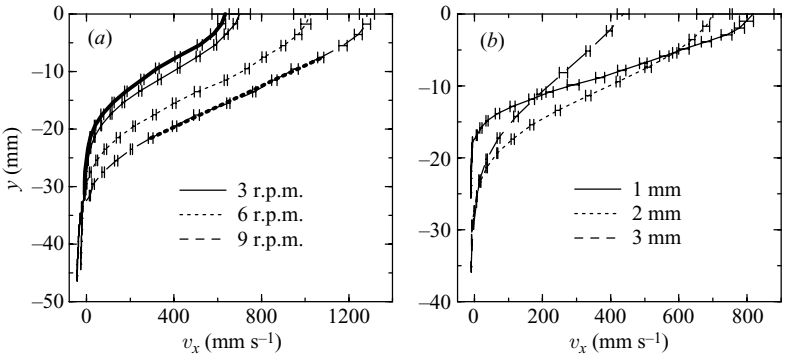


FIGURE 6. Variation in the x-component of the mean velocity, v_x, with depth y in the layer. (*a*) The thick solid line denotes the experimental data for 2 mm brass particles rotated at 3 r.p.m. The other lines denote the data for 2 mm SS balls at different rotational speeds. The thick dotted line shows a straight line fit to the linear portion of the 9 r.p.m. profile. (*b*) The thick solid line denotes the data for 1 mm SS balls rotated at 2 r.p.m. The other lines denote the data for SS balls rotated at 3 r.p.m. The error bars denote the standard deviation over 10 sets.

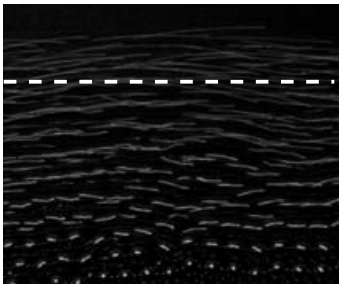


FIGURE 7. Typical time-lapse image showing the ballistic trajectories of particles in the low-density region (above the dashed line).

cylinder, assuming that the bulk densities in the bed and the layer are the same, yields $q = \omega R^2/2$; the calculated values are given in table 2. Increasing the rotational speed is thus equivalent to increasing the local flow rate.

The variation in the x-component of the mean velocity, v_x, with depth y in the layer is shown in figure 6 for different rotational speeds, particle sizes and materials studied. The error bars denote the standard deviation over 10 different data sets. All the measured quantities are plotted from $y = 0$ at the free surface of the flow down to about 3–4 particle diameters below the point corresponding to the minimum absolute velocity. The free surface is taken to be the level at which the measured number density is close to zero ($n < 10^{-3}$ mm^{-2}). The profiles are linear over most of the layer depth for all the cases studied, with an exponential decay near the base of the flowing layer. The negative velocities correspond to particles in the rotating bed which move in a direction opposite to that of the flowing layer. Further, the profiles tend to flatten out near the free surface. This is a low-density region comprising saltating particles. The ballistic trajectories in this region are clearly seen in figure 7, which is an image of the flow taken at a low shutter speed.

The magnitude of the maximum velocity and the depth of the layer increase with the rotational speed for a fixed particle size (figure 6*a*). The length of the central linear region of the velocity profile increases with increasing rotational speed, while

https://doi.org/10.1017/S002211200600320X Published online by Cambridge University Press

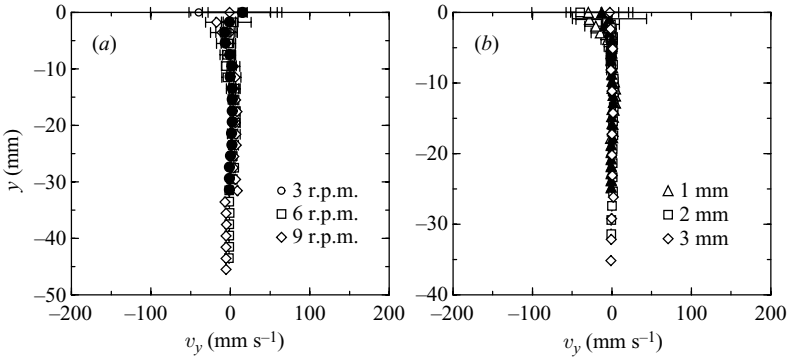


FIGURE 8. Variation in the y-component of the mean velocity, v_y, with depth y in the flowing layer. (*a*) The open symbols denote the experimental data for 2 mm SS balls. The solid symbols denote the data for 2 mm brass particles rotated at 3 r.p.m. (*b*) The open symbols denote the experimental data for SS balls for a rotational speed of 3 r.p.m. The solid symbols denote the data for 1 mm SS balls rotated at 2 r.p.m. The error bars denote the standard deviation over 10 sets.

the length of the exponential region near the bottom of the layer is nearly constant for all the cases considered. The shear rate $\dot{\gamma} = \mathrm{d}v_x/\mathrm{d}y$ corresponding to the linear portion increases with rotational speed. The profiles for SS and brass particles are close to each other, indicating that particle material parameters such as the coefficient of restitution and the particle roughness have a minor effect on the flow. This is in agreement with our earlier work (Orpe & Khakhar 2001) and that of Jain *et al.* (2002) on rotating cylinders. The maximum velocity decreases and the depth of the flowing layer increases with increasing particle diameter for a fixed rotational speed (figure 6*b*). The shear rate thus decreases with increasing particle size.

Qualitatively similar velocity profiles have been reported in the literature for different experimental systems. A linear and an exponential region of the velocity profile was observed in rotating cylinders for various rotational speeds studied (Bonamy *et al.* 2002*a*; Longo & Lamberti 2002; Zanuttigh & Lamberti 2002). The trends obtained in figure 6*b* for varying particle size are similar to those reported by Jain *et al.* (2002). The system size used in all these cases was comparable with our experimental system. The velocity profile in the lower half of the layer resembles the profiles obtained by Mueth *et al.* (2000) and Bocquet *et al.* (2001) for Couette flows. In some of the studies mentioned above (Rajchenbach *et al.* 1995; Bonamy *et al.* 2002*a*), the flattened upper low-density region was not obtained.

The magnitude of the y-component of the mean velocity, v_y, was close to zero throughout the depth of the layer for all the cases considered (figure 8) and the variations are within the experimental error. This confirms that the flow is nearly unidirectional in the region of measurement. The profiles of the projected area fraction of the particles, $\phi = N\pi d^2/4A$, where N is the number of particles counted per bin and A is the area of the bin, are shown in figure 9. The area fraction is nearly constant over the entire layer, with a rapid drop near the free surface. There is no significant variation in the magnitude of the area fraction (relative to the measurement error) for the different rotational speeds and materials. The area fractions are significantly smaller than the hexagonal-close-packed limit, $\phi_c = 0.866$. Nearly constant surface densities across the flowing layer were also observed by Rajchenbach *et al.* (1995), Bonamy *et al.* (2001) and Jain *et al.* (2002).

https://doi.org/10.1017/S002211200600320X Published online by Cambridge University Press

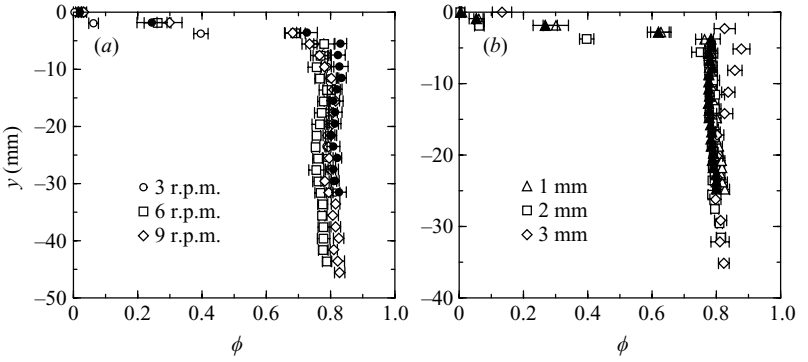


FIGURE 9. Variation in the area fraction ϕ with depth y in the flowing layer. (*a*) The open symbols denote the experimental data for 2 mm SS balls. The solid symbols denote the data for 2 mm brass particles rotated at 3 r.p.m. (*b*) The open symbols denote the experimental data for SS balls for a rotational speed of 3 r.p.m. The solid symbols denote the data for 1 mm SS balls rotated at 2 r.p.m. The error bars denote the standard deviation over 10 sets.

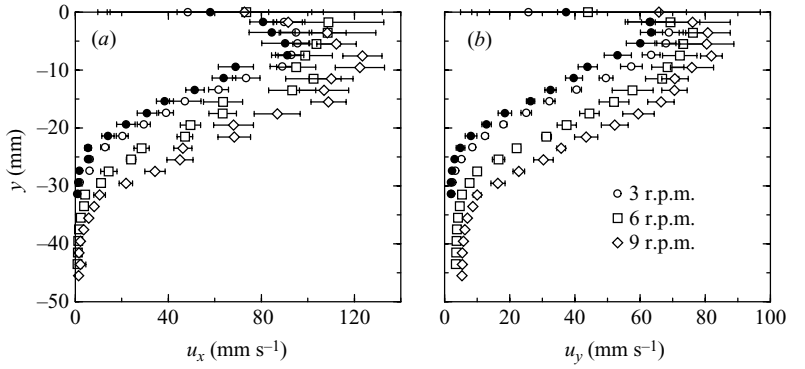


FIGURE 10. Variation in the components of the r.m.s. velocity with depth in the flowing layer. The open symbols denote the experimental data for 2 mm SS balls. The solid symbols denote the experimental data for 2 mm brass particles rotated at 3 r.p.m. The error bars denote the standard deviation over 10 sets.

The components of the r.m.s. velocities u_x and u_y across the flowing layer are shown in figures 10 and 11. In both cases, the r.m.s. velocity profiles are nearly linear over a large portion of the layer, with a flattening near the free surface and an exponential decay near the base of the flowing layer. The sizes of the flattened region as well as the region of exponential decay are larger for the r.m.s. velocity profiles than the corresponding regions for the mean velocity profiles. The r.m.s. velocities are smaller by nearly an order of magnitude than the mean velocities. The relative error is thus larger in this case than in the case of the mean velocities, as indicated by the error bars. The r.m.s. velocities increase with rotational speed for a fixed particle size. The slope of the linear region in each case is nearly independent of the rotational speed but increases with particle diameter (i.e. $\mathrm{d}u_x/\mathrm{d}y$, $\mathrm{d}u_y/\mathrm{d}y$ decrease). The r.m.s. velocities for the brass balls are quite close to those for steel, which again indicates that the flow behaviour is nearly independent of the material properties. The anisotropy in the r.m.s. velocities is clearly evident from the graphs and the r.m.s. velocity component in the flow direction is larger by about 50% than that normal to the flow direction.

https://doi.org/10.1017/S002211200600320X Published online by Cambridge University Press

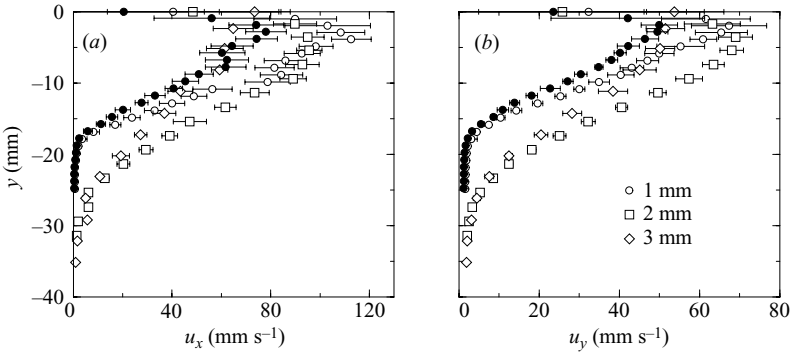


FIGURE 11. Variation in the components of the r.m.s. velocity with depth, in the flowing layer. The open symbols denote the data for SS balls rotated at 3 r.p.m. The solid symbols denote the data for 1 mm SS balls rotated at 2 r.p.m. The error bars denote the standard deviation over 10 sets.

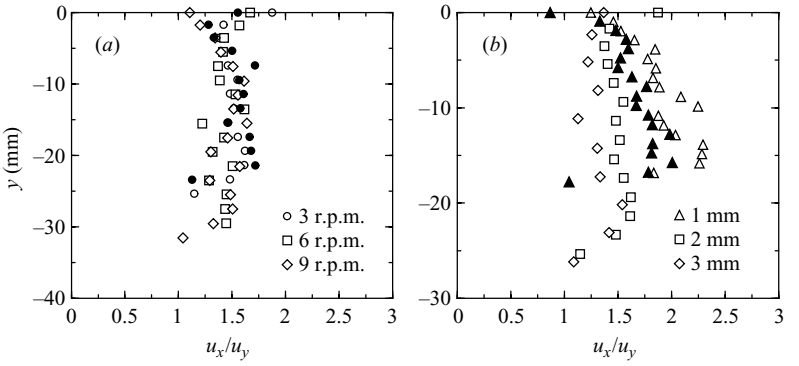


FIGURE 12. Variation in the ratio of the r.m.s. velocity components across the flowing layer. (*a*) The open symbols denote-data for 2 mm SS balls. The solid symbols denote the data for 2 mm brass particles. (*b*) The open symbols denote the data for SS balls rotated at 3 r.p.m. The solid symbols denote the data for 1 mm SS balls rotated at 2 r.p.m.

A linear and a flattened region in the r.m.s. velocity profiles was also obtained by Jain *et al.* (2002) in their experiments in rotating cylinders but they found the r.m.s. velocities to be about one-third of the mean velocity near the free surface. These values are significantly larger than the r.m.s. velocities obtained here.

The degree of anisotropy in the r.m.s. velocities across the flowing layer for all the cases studied is shown in figure 12. The ratio u_x/u_y is nearly constant (≈ 1.5) across the flowing layer and is independent of rotational speed while it decreases slightly with an increase in the particle diameter. The data for brass and SS balls is nearly the same. Azanza, Chevoir & Moucheront (1999) found the ratio of the r.m.s. velocity components to be 1.45 for two-dimensional chute flows, while a ratio of 1.3 was obtained by Bocquet *et al.* (2001) for Couette flows. Anisotropy in the r.m.s. velocity components was also observed by Jain *et al.* (2002) for experiments with rotating cylinders.

We may obtain the stress profiles in the flowing layer from a stress balance, taking into account the contribution of wall friction. Assuming the flow to be steady and

https://doi.org/10.1017/S002211200600320X Published online by Cambridge University Press

fully developed, the Cauchy equations averaged across the gap width b are

$$0 = \frac{\mathrm{d}\langle\tau_{yx}\rangle}{\mathrm{d}y} + \frac{1}{b}\tau_{zx}\Big|_0^b + \langle\rho\rangle g \sin\beta_m, \tag{3.1a}$$

$$0 = \frac{\mathrm{d}\langle\tau_{yy}\rangle}{\mathrm{d}y} - \langle\rho\rangle g \cos\beta_m, \tag{3.1b}$$

where $\langle\cdot\rangle = (1/b)\int_0^b \cdot\,\mathrm{d}z$ denotes an average across the gap. The stress at the side walls due to friction is

$$\tau_{zx}|_0 = -\tau_{zx}|_b = \tau_{zz}\mu_w, \tag{3.2}$$

where μ_w is the coefficient of wall friction. The latter is assumed to be a constant, which may overestimate the actual value. Assuming further that the variation in the stresses across the gap is small, that the normal stresses are isotropic ($\tau_{zz} = \tau_{yy}$) and that the stresses vanish at the free surface we obtain

$$\tau_{yy} = \rho_b \cos\beta_m \int_{-y}^{0} (\phi/\phi_b)\,\mathrm{d}y, \tag{3.3a}$$

$$\tau_{yx} = \rho_b \sin\beta_m \int_{-y}^{0} (\phi/\phi_b)\,\mathrm{d}y - 2\mu_w/b \int_{-y}^{0} \tau_{yy}\,\mathrm{d}y. \tag{3.3b}$$

In the above equations ϕ_b is taken to be the constant value near the base of the flowing layer (figure 9). The bulk density in the rotating bed is obtained as $\rho_b = (1/2)m_b/\pi R^2 b$, from the measured mass of particles in the half-filled cylinder, m_b; the results are given in table 1. The effective coefficient of friction for the particles at the base of the layer is obtained from (3.3) as

$$\mu_i = \frac{\tau_{yx}}{\tau_{yy}} = \tan\beta_m - \mu_w \frac{\delta_e}{b}, \tag{3.4}$$

where $\delta_e = 2\int_{-y_s}^{0} \tau_{yy}\,\mathrm{d}y]/[\rho_b \int_{-y_s}^{0} (\phi/\phi_b)\,\mathrm{d}y]$ is the effective layer thickness and y_s is the position of the base of the layer, which we take to be the point at which the shear rate extrapolates to zero. Equation (3.4) is identical to one obtained by Taberlet *et al.* (2003) if δ_e is replaced by the measured layer thickness δ. Here we obtain δ_e by numerical integration of the experimental profiles to avoid the ambiguity in defining the location of the free surface.

Equation (3.4) allows the estimation of the wall friction coefficient from experimental data. Figure 13 shows a plot of the measured values of $\tan\beta_m$ versus δ_e/b for all the cases studied. All the data at 3 r.p.m. (open symbols), corresponding to a fixed flow rate, fall on a straight line, which yields a wall friction coefficient of $\mu_w = 0.09$, which is a reasonable value for steel beads on a smooth surface. The data for higher rotational speeds (solid symbols), which correspond to significantly higher flow rates, deviate from the fitted straight line. Analysis of the data for cylinders of different diameters and for a wider range of flow rates indicates that (3.4) holds, but unrealistically high values of μ_w are obtained ($\mu_w > \mu_i$ in some cases) (Khakhar, Orpe & Hajra 2005). The physical cause for the high values of $\tan\beta_m$ obtained here and previously is not known. It may be because μ_w is dependent on velocity or because μ_i is dependent on velocity and needs to be further investigated. However, since the correction for wall friction is small over most of the layer, in the data reported here we correct the shear stress using the value 0.09 for the wall friction coefficient μ_w in all cases.

https://doi.org/10.1017/S002211200600320X Published online by Cambridge University Press

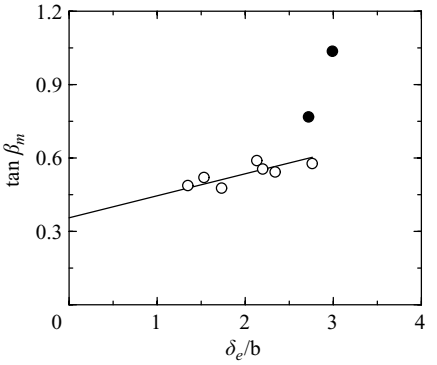


FIGURE 13. Variation in the coefficient of static friction, $\tan\beta_m$, with the scaled effective layer thickness δ_e. Open symbols, data for 3 r.p.m.; filled symbols, data for 6 and 9 r.p.m. The line is the least-squares fit to the 3 r.p.m. data.

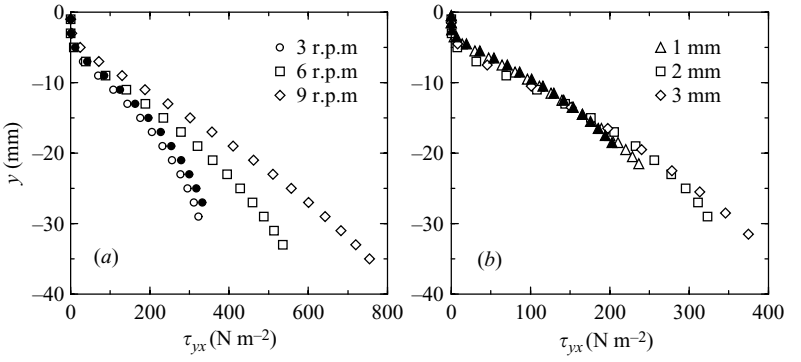


FIGURE 14. Shear stress (τ_{yx}) profiles in the flowing layer. (*a*) The open symbols denote the data for 2 mm SS balls. The filled symbols denote the data for 2 mm brass particles rotated at 3 r.p.m. (*b*) The open symbols denote the data for SS balls rotated at 3 r.p.m. The filled symbols denote the data for 1 mm SS balls rotated at 2 r.p.m.

The profiles for the shear stress are shown in figure 14. The stresses are linear across most of the layer with a slight curvature near the free surface and a deviation from linearity deeper in the layer due to wall friction. The linear variation results from the nearly constant area fraction ϕ over most of the layer. The shear stress increases with the angular speed (figure 14*a*), while the normal stress shows the opposite trend. The reason is that β_m increases with angular speed. The shear-stress profile is nearly independent of the particle size d and the material type (figure 14*b*).

The components of the streaming-stress contribution to the total stress tensor are (Campbell 1990)

$$\tau^k_{yx}(y) = \rho(\overline{c_x c_y} - \overline{c_x}\,\overline{c_y}), \tag{3.5a}$$

$$\tau^k_{xx}(y) = \rho(\overline{c_x c_x} - \overline{c_x}\,\overline{c_x}), \tag{3.5b}$$

$$\tau^k_{yy}(y) = \rho(\overline{c_y c_y} - \overline{c_y}\,\overline{c_y}), \tag{3.5c}$$

where c_x and c_y are the components of the instantaneous velocities for all the relevant particles and for every y-coordinate and ρ is the nearly constant layer density. The profiles of the streaming component of the shear stress normalized by the total

https://doi.org/10.1017/S002211200600320X Published online by Cambridge University Press

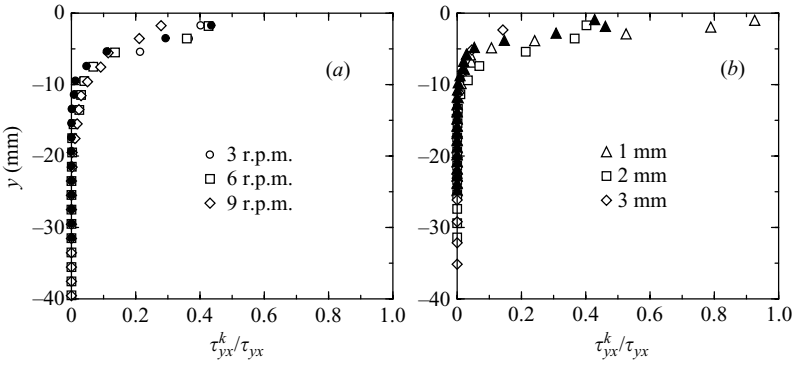


FIGURE 15. Variation in the ratio of the streaming stress τ^k_{yx} and the total shear stress τ_{yx} with depth y in the flowing layer. (*a*) The open symbols denote the data for 2 mm SS balls. The filled circles denote the data for 2 mm brass particles rotated at 3 r.p.m. (*b*) The open symbols denote the data for SS balls rotated at 3 r.p.m. The filled triangles denote the data for 1 mm SS balls rotated at 2 r.p.m.

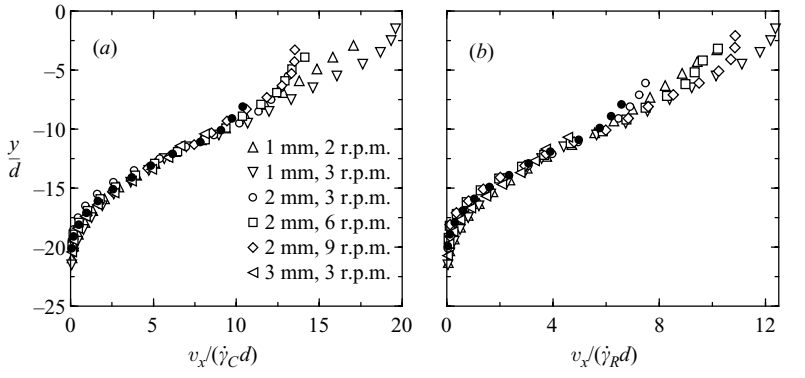


FIGURE 16. Variation in the rescaled mean velocity with rescaled depth in the flowing layer. The filled symbols denote the data for brass particles rotated at 3 r.p.m. The data for all sets are shifted after scaling so as to superimpose the profiles. (*a*) Scaling based on the shear rate given by (1.1). (*b*) Scaling based on the shear rate of Rajchenbach (2003).

shear stress are shown in figure 15. Very similar profiles are obtained for the normal stresses. Streaming stresses are a significant component of the total stress near the free surface and are more than 20% of the total stress in the region corresponding roughly to the flattened portion in the r.m.s. velocity profiles. Deeper in the bed the streaming stresses become negligibly small. This behaviour is consistent with the observed particle trajectories (figure 7) and the density profile (figure 9).

3.2. *Scaling and analysis*

We rescale the velocity profiles using a characteristic velocity $v_C = \dot\gamma_C d$, with the characteristic shear rate $\dot\gamma_C = [g \sin((\beta_m - \beta)/d \cos\beta_s)]^{1/2}$ based on (1.1), and use the particle diameter d as the characteristic length. After rescaling, the dimensionless profiles are shifted in the y-direction so as to superimpose the profiles. The resulting profiles are shown in figure 16(*a*). All the profiles for different rotational speeds, particle sizes and material types collapse to a single curve. The linear regions of the profiles, in particular, superimpose very well. The scaling thus describes the variation of the mean velocity profiles with particle diameter and local flow rate quite

https://doi.org/10.1017/S002211200600320X Published online by Cambridge University Press

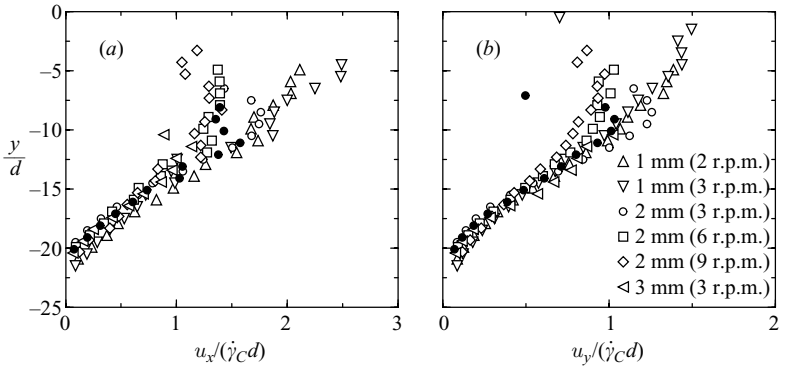


FIGURE 17. Scaled profiles of the components of the r.m.s. velocity in the flowing layer. The filled symbols denote the data for brass particles rotated at 3 r.p.m.

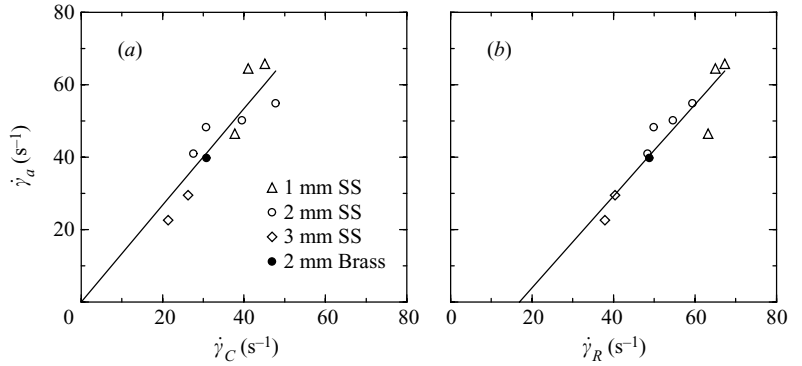


FIGURE 18. (*a*) The measured average shear rate $\dot{\gamma}_a$ and the shear rate $\dot{\gamma}_c$ predicted from Khakhar *et al.* (2001*a*). (*b*) The measured average shear rate $\dot{\gamma}_a$ and the shear rate $\dot{\gamma}_R$ predicted from Rajchenbach (2003). The symbols show the experimental data for all the cases studied. The solid lines show linear fits to the data.

well. Figure 16(*b*) shows the same data but rescaled by the characteristic velocity based on the shear rate proposed by Rajchenbach (2003), $\dot{\gamma}_R = (g \sin \beta_m / d)^{1/2}$. The scaled profiles superimpose equally well in this case, after appropriately translating the profiles in the y-direction. From the data available it is difficult to distinguish between the two relations for the shear rate.

The r.m.s. velocity profiles scaled using the characteristic shear rate $\dot{\gamma}_C$ and shifted by the same distance as that for the mean velocity profiles are shown in figure 17(*a*). The scaled profiles collapse to a single curve over most of the layer except for the region near the free surface, though the relative scatter in this case is greater then that for the mean velocity profile.

We define an average shear rate for a velocity profile, $\dot{\gamma}_a$, as the velocity gradient obtained by fitting a straight line to the linear portion of the velocity profile. An example of such a fit is shown in figure 6(*a*). We note that the magnitude of the shear rate varies depending on the number of points included in the fitting. This variation is, however, less than 10% when the number of points that are assumed to lie in the 'linear' portion is varied. Figure 18(*a*) shows the measured shear rates and the characteristic shear rate $\dot{\gamma}_C$ for comparison. Although there is scatter in the data, there is reasonable agreement between the model predictions and experiment.

https://doi.org/10.1017/S002211200600320X Published online by Cambridge University Press

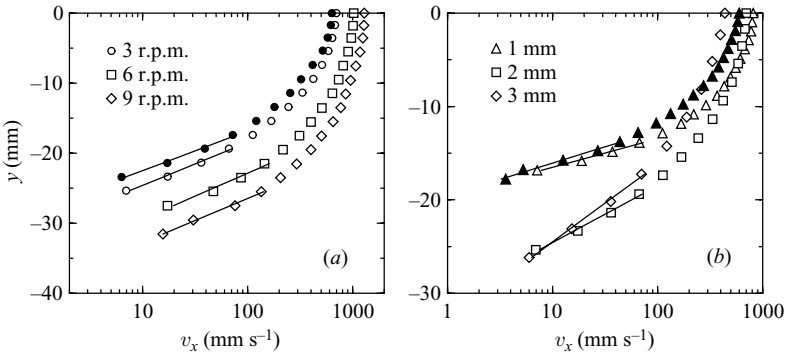


FIGURE 19. Profiles of the mean velocity v_x across the flowing layer plotted on a semi-log scale. The solid lines show exponential fits to the linear portions of the profiles. (*a*) The open symbols denote the data for 2 mm SS balls. The filled circles denote the data for 2 mm brass particles rotated at 3 r.p.m. (*b*) The open symbols denote the data for SS balls rotated at 3 r.p.m. The filled triangles denote the data for 1 mm SS balls rotated at 2 r.p.m.

A least-squares fit gives $c = 0.56$, which is different from the value $c \approx 1.5$ estimated by Orpe & Khakhar (2001). The latter value was based on shear rates calculated assuming a linear velocity profile across the entire flowing layer. The velocity profiles are actually linear only in the central region of the layer and the shear rates are lower near the free surface and the bed. The shear rates calculated by Orpe & Khakhar (2001) are, thus, lower than the values corresponding to the central linear part, which results in a higher value for c.

The average shear rate $\dot{\gamma}_a$ is also proportional to the shear rate $\dot{\gamma}_R$ proposed by Rajchenbach (2003), as shown in figure 18(*b*). However, a linear fit gives a significant negative intercept, with $\dot{\gamma}_a = 1.26(\dot{\gamma}_R - 16.9)$. This comparison indicates that $\dot{\gamma}_C$ may give a better description of the flow than $\dot{\gamma}_R$.

A semi-log plot of the velocity profile indicates that the exponential region of the velocity profile spans 3–4 particle diameters (figure 19). We fit straight lines to this data to obtain the characteristic decay length λ, defined by

$$v_x = v_0 \mathrm{e}^{-y/\lambda}, \tag{3.6}$$

where v_0 is a constant of proportionality. The variation in the characteristic length λ with the particle diameter d for the different cases studied is shown in figure 20(*a*). The values of λ depend on the particle size d, but are nearly independent of the rotational speed and material type. A linear fit to the data yields $\lambda/d = 1.1 \pm 0.2$. This result indicates a relatively sharp decay of the velocity with depth in the bed since the characteristic length is just a little more than one particle diameter. A linear variation in the characteristic decay length with particle diameter was obtained by Komatsu *et al.* (2001) for the exponential region in heap flow. A significantly larger characteristic length ($10d$) was obtained by Mohan *et al.* (1997) for dense flows in a vertical channel.

An exponential decay is also found for the portion of the r.m.s. velocities near the base of the layer. A plot of the characteristic length versus the particle diameter obtained from fits to the r.m.s. velocity u is shown in figure 20(*b*). A linear fit to the data yields $\lambda/d = 1.7 \pm 0.3$. Thus the r.m.s. velocity decays slightly more slowly with depth than the mean velocity.

https://doi.org/10.1017/S002211200600320X Published online by Cambridge University Press

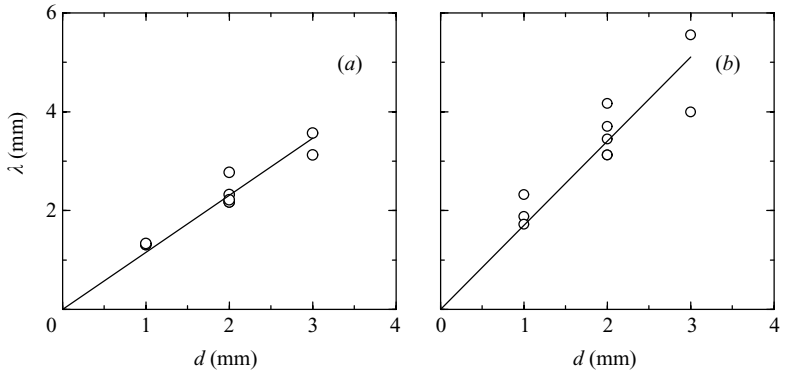


FIGURE 20. Variation in the characteristic length λ in an exponential fit vs. particle diameter d for (a) the mean velocity profile, (b) the r.m.s. velocity profile.

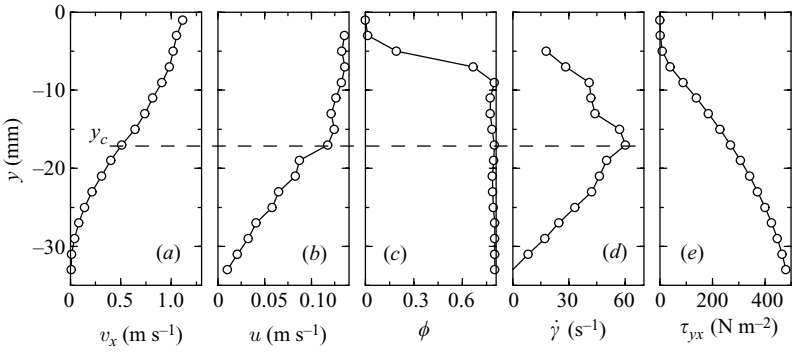


FIGURE 21. Profiles of the mean velocity v_x, the r.m.s. velocity u, the area fraction (ϕ), the shear rate $\dot{\gamma}$ and the shear stress τ_{yx} in the flowing layer for 2 mm SS balls rotated at 6 r.p.m. The dashed line denotes the transition depth y_c.

3.3. *Rheology*

The variations in the measured quantities with depth in the layer for one case are shown side by side in figure 21 to give an overall qualitative view of the rheology. The shear-rate profile, obtained by numerical differentiation of the mean velocity profile (i.e. $\dot{\gamma}(y) = \mathrm{d}v_x/\mathrm{d}y$), is shown in figure 21(d). For all the cases studied, the shear rate increases to a maximum with increasing depth and then decreases as the fixed bed is approached. We note that a relatively smooth curve is obtained as a result of averaging with a bin size equal to the particle diameter. An oscillating shear-rate profile is obtained, as reported in previous works (Mueth *et al.* 2000; Mueth 2003 Hill, Gioia & Tota 2003). if a smaller bin size is used. The fluctuations in the shear-rate profile arise from the magnification of errors resulting from taking a derivative of the velocity-profile data. The fluctuations are larger for higher rotational speeds and smaller particles. The results indicate that the velocity profile is not linear anywhere in the flowing layer, although the region around the maximum may be approximated to be linear. The shear rate decreases to a small value near the free surface.

The graphs in figure 21 indicate that on the basis of its rheological behaviour, the layer can be considered to comprise two regions with different flow characteristics. Above a critical depth y_c, corresponding to the depth of the shear-rate maximum, the shear stress increases with shear rate. However, in the region below y_c the trend

https://doi.org/10.1017/S002211200600320X Published online by Cambridge University Press

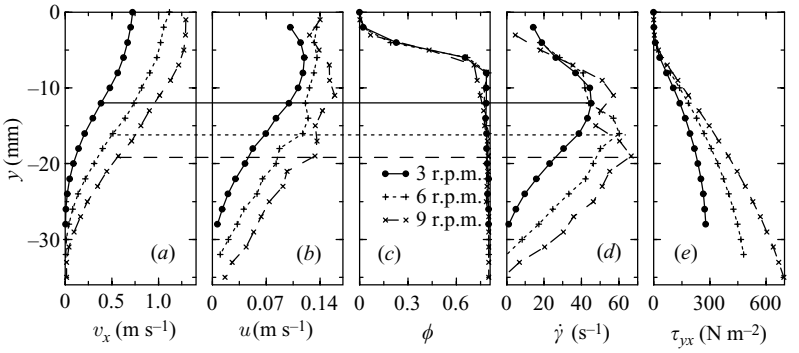


FIGURE 22. Profiles of the mean velocity v_x, the r.m.s. velocity u, the area fraction ϕ, the shear rate $\dot{\gamma}$ and the shear stress τ_{yx} in the flowing layer for 2 mm SS balls at different rotational speeds. The horizontal lines denote the transition depth for each rotational speed.

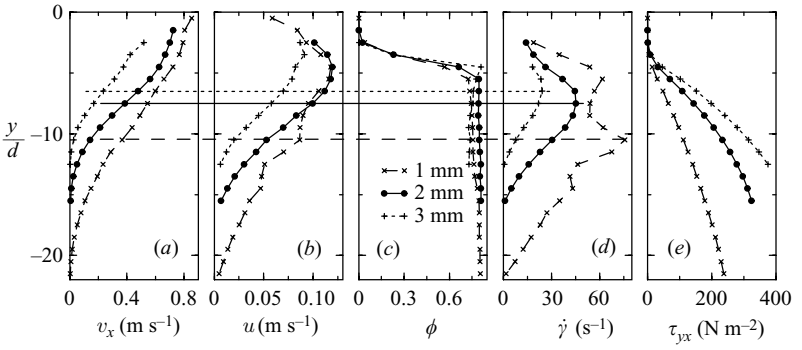


FIGURE 23. Profiles of the mean velocity v_x, the r.m.s. velocity u, the area fraction ϕ, the shear rate $\dot{\gamma}$ and the shear stress τ_{yx} in the flowing layer for different diameter SS balls at 3 r.p.m. The horizontal lines denote the transition depth for each particle size.

is reversed and the shear stress increases while the shear rate decreases. There also appears to be a transition in the r.m.s. velocity at y_c: above y_c the profile is nearly flat, whereas it decreases with depth below y_c. Similar results are obtained for all cases studied.

Figure 22 shows, for comparison, profiles for 2 mm particles and various cylinder rotational speeds. All graphs for a particular rotational speed are shifted along the y-axis so that the area-fraction profiles are superimposed. This ensures that the free surface in all cases is located at the same y-position, so that depths may be compared. The transition in the flow is seen in all the cases considered and the data indicate that y_c increases with rotational speed. Figure 23 shows, for comparison, profiles for different-diameter particles rotated at 3 r.p.m. In this case the depth is rescaled by the particle diameter before the graphs are shifted to superimpose the area-fraction profiles. The results indicate that the scaled depth decreases with increasing particle diameter. Finally, figure 24 shows data for 3 mm particles for two values of the gap width b. Although the mean velocity and r.m.s. velocity profiles are slightly different for the two gaps, the transition depth does not depend on the gap width.

Evidence for transition in the flow is also seen in the velocity distributions. Figure 25 shows the velocity distributions at different locations in the layer for 2 mm particles rotated at 3 r.p.m. The distributions vary significantly with depth in the layer. The

https://doi.org/10.1017/S002211200600320X Published online by Cambridge University Press

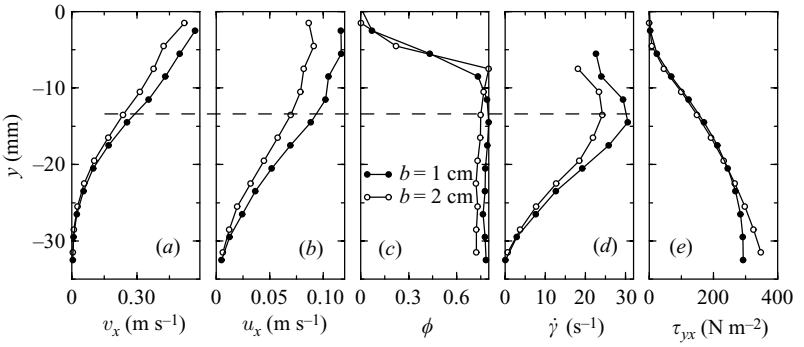


FIGURE 24. Profiles of the mean velocity v_x, the r.m.s. velocity u, the area fraction ϕ, the shear rate $\dot{\gamma}$ and the shear stress τ_{yx} across the flowing layer for 3 mm SS balls at 3 r.p.m. for different gap widths b. The dashed horizontal line denotes the transition depth.

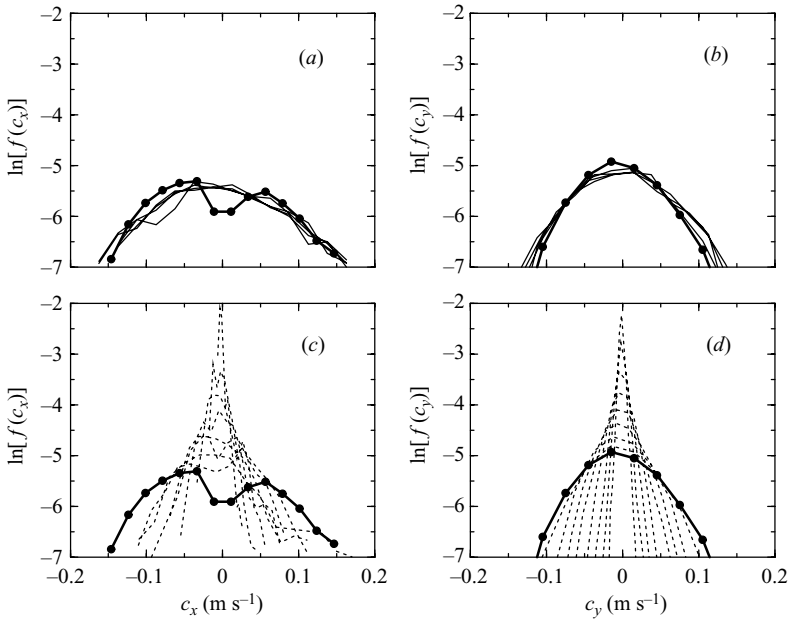


FIGURE 25. Velocity distributions at different depths in the layer for 2 mm SS balls rotated at 3 r.p.m. The thick solid line with filled circles represents the data at the transition point. (*a*), (*b*) The region at and above the transition point. (*c*), (*d*) The region at and below the transition point.

c_y-distribution is Gaussian for all points above the transition point, $y \geqslant y_c$ (figure 25*b*). Below the transition point, $y < y_c$, it gradually evolves to a Poisson distribution with increasing depth in the layer (figure 25*d*). The c_x-distribution is Gaussian above the transition point (figure 25*a*). However, at and below the transition point the behaviour is complex and bimodal distributions are obtained at varying locations in the layer (figure 25*c*). Similar behaviour is obtained for all the cases studied. The c_y-distributions below the transition point are qualitatively similar to the distributions obtained by Mueth (2003) for dense Couette flow.

https://doi.org/10.1017/S002211200600320X Published online by Cambridge University Press

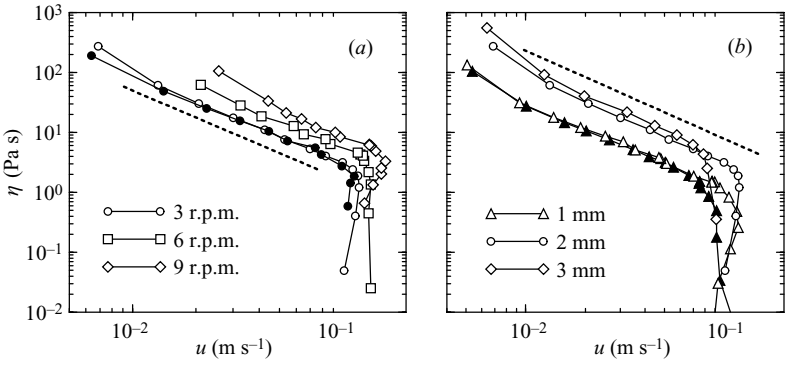


FIGURE 26. Apparent viscosity η vs. r.m.s. velocity u for the different cases studied. (*a*) The open symbols represent the experimental data for 2 mm SS balls. The filled circles represent the data for 2 mm brass particles rotated at 3 r.p.m. (*b*) The open symbols represent experimental data for the SS balls rotated at 3 r.p.m. The filled triangles represent the data for 1 mm SS balls rotated at 2 r.p.m. The dotted lines represent a least-squares fit (slope ≈ -1.5) to the data in the linear region.

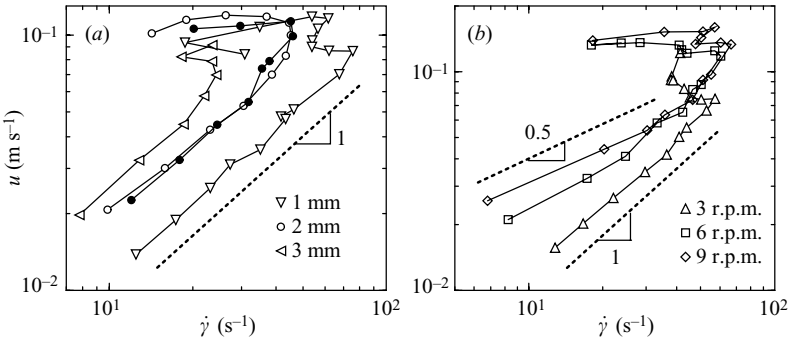


FIGURE 27. Variation of the r.m.s. velocity u with the shear rate $\dot{\gamma}$ in the the flowing layer. Dotted lines show least-squares fits to the linear portions of the graphs. (*a*) Particles of different diameter and a rotational speed of 3 r.p.m. The solid symbols denote the data for 2 mm brass particles. (*b*) 2 mm particles at different rotational speeds.

In the region below the transition depth y_c, the decrease in shear rate with depth, accompanied by an increase in shear stress with depth, implies a sharp increase in the apparent viscosity, defined as $\eta = \tau_{yx}/\dot{\gamma}$. Figure 26 shows the variation in the apparent viscosity η with the r.m.s. velocity u. The granular temperature is $T = u^2$; thus the variation in figure 26 may be considered to be analogous to the variation of viscosity with temperature in molecular fluids. The viscosity varies by more than three orders of magnitude and all the data show qualitatively similar behaviour. Near the free surface the viscosity is low and increases at constant u, essentially owing to the increase in the volume fraction of solids. Below the transition point there is a gradual increase in viscosity with depth corresponding to a decreasing u. The variation in η with u in the region just below the transition in all cases is power-law, with an exponent of about -1.5. At lower values of u the curves turn upward and the rate of increase in η appears to become higher.

Figure 27 shows the variation in the r.m.s. velocity u with shear rate $\dot{\gamma}$. There is a power-law dependence of the two in the region below the transition to the

https://doi.org/10.1017/S002211200600320X Published online by Cambridge University Press

d (mm)	ω (r.p.m.)	δ_f (mm)	δ_s (mm)
1	3	6	11
2	3	7	16
2	6	11	16
2	9	14	15
3	3	7	20

TABLE 3. Measured thicknesses δ_f and δ_s of the fluid-like and solid-like layers for the different cases.

high-density region. The exponent α is independent of the particle diameter (figure 27*a*) but appears to decrease systematically with increasing r.p.m., ranging from $\alpha = 1$ for low rotational speeds to $\alpha = 0.5$ for 9 r.p.m. For $\alpha = 1$ we have $u \propto \dot{\gamma}$, which is consistent with a physical picture according to which fluctuations should depend on local relative motion. A power-law variation between the r.m.s. velocity and the shear rate have been obtained previously by Bocquet *et al.* (2001) and Mueth (2003) for dense Couette flows. The value of the exponent reported by them is around $\alpha = 0.5$. Azanza *et al.* (1999) found $\alpha = 1$ for rapid flows.

The above results indicate the presence of two regimes in the flowing layer, with a sharp transition point. In the upper region near the free surface the behaviour is fluid-like and the velocity distributions are Maxwellian. Below the transition point the material appears to be an amorphous soft solid, increasing in strength with depth in the layer. The transition to this solid-like regime occurs at a relatively large r.m.s. velocity ($\approx 0.1\,\mathrm{m\,s^{-1}}$). Qualitatively similar behaviour is obtained for different particles and operating speeds.

We conjecture that the sharp transition occurs because of the formation of a percolated network of particles in extended contact with each other. This is in contrast with the fluid-like regime where the particles interact through collisions. The contact network coexists with fluid-like domains and the fraction of particles which are part of the network increases with depth. This picture for the region below the transition point is broadly consistent with recent measurements of Bonamy *et al.* (2002*b*), in which flowing clusters were identified, as well as with non-local models based on the coexistence of particle chains and fluid-like material (Mills *et al.* 1999; Bonamy & Mills 2003).

Table 3 gives the thickness of the fluid-like (δ_f) and solid-like (δ_s) regions obtained from the data in figures 22 and 23. The data indicates that δ_f is independent of the particle diameter but depends on the rotational speed (i.e. the local flow rate q). In contrast, δ_s is independent of the r.p.m. but proportional to the particle diameter ($\delta_s \approx 6.7 + 4.5d$ mm). The latter result is consistent with the finding that the characteristic length λ for exponential decay of the velocity is proportional to diameter but independent of rotational speed. The physical picture that emerges is that the solid-like layer is formed first, its maximum thickness being determined by the particle diameter. When the local flow rate exceeds some critical value determined by the maximum solid-like-layer thickness, the excess goes to form the liquid-like layer. The data of Courrech-DuPont *et al.* (2005) for transient flow in a rotating cylinder perhaps correspond to flow rates below the critical value and hence only the exponential region is seen. We note that a different scaling for the layer thickness is obtained if a macroscopic viewpoint is considered in which the velocity profile is assumed to be linear and the region of exponential decay of the velocity is neglected.

https://doi.org/10.1017/S002211200600320X Published online by Cambridge University Press

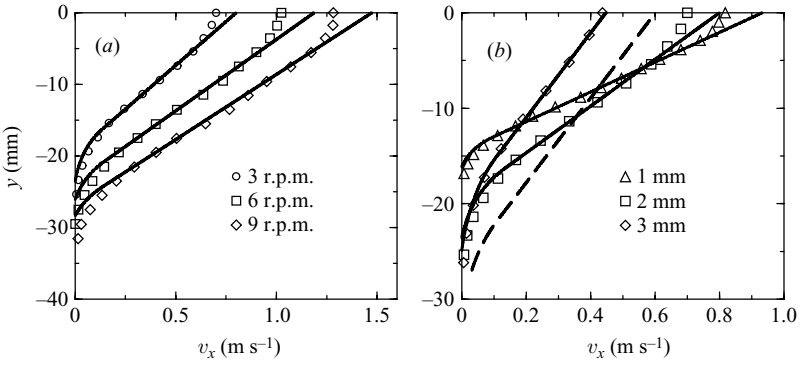


FIGURE 28. Profiles of the mean velocity v_x in the flowing layer. The solid lines show the predictions of the model of Bonamy & Mills (2003). (*a*) The symbols denote the data for 2 mm SS balls. (*b*) The symbols denote the data for SS balls rotated at 3 r.p.m.

In this case, based on the characteristic shear rate for the layer given by (1.1), we get $\delta \propto d^{1/4}$, which is verified in figure 18.

3.4. *Comparison with theory*

Bonamy & Mills (2003) proposed a non-local model for the surface flow of granular material, based on an earlier work by Mills *et al.* (1999). The model regards the flowing granular medium as a network of transient particle chains immersed in an assembly of particles behaving as a viscous Newtonian fluid. The stresses are then propagated through these chains in a non-local manner. The total stress is expressed as a linear combination of Coulombic frictional stresses, viscous stresses and stresses due to the embedded chains.

The model equations, simplified for the case of surface flows in rotating cylinders for low rotational speeds ω, when inertial stresses can be neglected, yield an analytical expression for the profile of the velocity component v_x (Bonamy & Mills 2003):

$$v_x(y) \simeq \begin{cases} \left(\frac{\lambda}{2}\right)\dot{\gamma}\,\mathrm{e}^{2\delta/\lambda}\mathrm{e}^{2y/\lambda} - \left(\frac{\omega}{2R}\right)(y^2+R^2), & y \in (-R,-\delta), \quad (3.7a) \\ \dot{\gamma}\left(y+\delta+\frac{\lambda}{2}\right) - \left(\frac{\omega}{2R}\right)(y^2+R^2), & y \in (-\delta,0), \quad (3.7b) \end{cases}$$

where λ is a function of the characteristic correlation length of the transient chains. The shear rate $\dot{\gamma}$ and the characteristic length λ are parameters of the model. Using the mass-balance equation at the centre of the cylinder gives the following expression for the layer thickness:

$$\delta \simeq R\left(\frac{4\omega}{3\dot{\gamma}}\right)^{1/2}. \quad (3.8)$$

Equations (3.4) and (3.8) are used to calculate the velocity profiles across the flowing layer. The shear rate in each case is taken to be the value obtained by fitting a straight line to the linear part of the experimental profile ($\dot{\gamma}_a$, figure 18). The values of the correlation length are found to be related to the particle diameter by $\lambda/d = 4$ for all cases.

The predicted and experimental profiles are shown in figure 28. The model predicts the exponential and the linear part of the velocity very well for all rotational speeds and particle sizes, but it does not predict the flattening of the profile near the

https://doi.org/10.1017/S002211200600320X Published online by Cambridge University Press

free surface. For the case of of 3 mm balls, the layer thickness calculated from (3.8) overpredicts the experimental layer thickness, resulting in a shift of the predicted profile (the dashed line in figure 28*b*). The reason for this mismatch is the experimental difficulty in correctly identifying the location of the free surface. If for this case we use the layer thickness value obtained from the experimental velocity profile, a good fit is obtained.

Aranson & Tsimring (2002) proposed an order-parameter description for the fluidization transition in granular flows. The order parameter specifies the fraction of the solid and fluid parts of the stress tensor and is related to the number of particles in contact with a given particle, on average (the coordination number). The dynamics of the order parameter p are assumed to be governed by the Ginzburg–Landau equation, which reduces in the case of a steady fully developed unidirectional flow to

$$0 = D\frac{\mathrm{d}^2 p}{\mathrm{d}y^2} - F(p,\mu), \tag{3.9}$$

where D is the characteristic diffusion coefficient for p. $F(p,\mu)$ is the derivative of the potential energy density and is given by

$$F(p,\mu) = (p-1)\{p^2 - 2p_* p + p_*^2 \exp[-A(\mu^2 - \mu_*^2)]\} \tag{3.10}$$

where $\mu = \tau_{yx}/\tau_{yy}$ and the quantities with asterisks are model parameters. Volfson, Tsimring & Aranson (2003) found $p_* = 0.6$, $A = 25$ and $\mu_* = 0.26$ from two-dimensional discrete-element simulations for $D = 2$. The fluid part τ_{yx}^f of the total shear stress τ_{yx} was obtained from simulations in terms of the order parameter as

$$\tau_{yx}^f = (1-p)^{2.5}\tau_{yx} = \eta\frac{\mathrm{d}v_x}{\mathrm{d}y}, \tag{3.11}$$

where η is the viscosity. Simulations for two-dimensional systems indicate $\eta = 12$. In the above equations (3.9)–(3.11) all quantities are made dimensionless using appropriate combinations of m, g and d.

We obtain the profile of the order parameter in the layer by numerical solution of (3.9) using a shooting method with the experimentally obtained profile for the local friction coefficient $\mu(y)$ as an input. The free surface is assumed to be a no-flux boundary for the order parameter ($D\mathrm{d}p/\mathrm{d}y = 0$ at $y = 0$) and pure solid ($p = 1$) is assumed far from the free surface ($y = \delta_A \gg 1$). The profiles are independent of the domain depth δ_A when it is large enough. The shear-rate ($\dot{\gamma} = \mathrm{d}v_x/\mathrm{d}y$) profile is then calculated from (3.11) using the experimentally obtained shear-stress profile.

The computed shear-rate profiles are shown, together with the experimentally measured profiles for comparison, in figure 29. This provides a more stringent test than matching the model to the measured velocity profiles. Predictions of the shear-rate profile using the parameters from two-dimensional simulations give only qualitative agreement with the experimental profiles. The results of one such calculation for 2 mm particles rotated at 3 r.p.m. is shown in figure 29 (long-dashed line) using the values given above for A, D and η, but taking $\mu* = 0.4$. The latter was necessary since no solution satisfying the boundary conditions was obtained for $\mu* = 0.26$ for the particular experimental profile for $\mu(y)$ used. We found excellent quantitative agreement between the model and the experimental results using $A = 5$ and $D = 2$ for four of the cases and $A = 10$ and $D = 2$ for one case, as shown in figure 29. However, different values of $\mu*$ and η are required to get a good fit and these are given in table 4. We found that $\mu*$ essentially determines the depth of the layer and thus it was adjusted to match the experimental and theoretical depths. The viscosity η

https://doi.org/10.1017/S002211200600320X Published online by Cambridge University Press

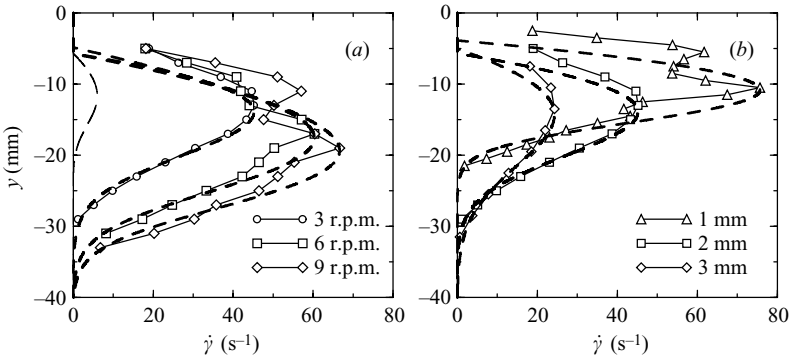


FIGURE 29. The shear-rate profiles predicted by the model of Aranson & Tsimring (2002) (dashed lines) compared with the measured shear-rate profiles. (*a*) The symbols denote the data for 2 mm SS balls. (*b*) The symbols denote the data for SS balls rotated at 3 r.p.m.

d (mm)	ω (r.p.m.)	A	$\mu*$	η	μ_i
1	3	5	0.36	0.97	0.36
2	3	5	0.40	0.85	0.34
2	6	5	0.57	1.74	0.52
2	9	5	0.81	2.77	0.77
3	3	10	0.41	0.84	0.37

TABLE 4. Values of fitting constants for the model of Aranson & Tsimring (2002), for the case of stainless steel. The values of the effective coefficient of friction at the base of the layer, $\mu_i = \mu(y_s)$, are also given.

is a proportionality factor and we calculated it as the ratio of the maximum computed shear rate to the maximum experimental shear rate for each profile. Once A and D are fixed, the calculated values of $\mu*$ and η are thus uniquely determined. The parameter A did not significantly affect the shape of the profiles when varied over a significant range ($A \in (5, 25)$) but determined the range of $\mu*$ for which solutions satisfying the boundary conditions could be obtained. Similarly, changing D over narrow ranges close to $D = 2$ did not change the profiles significantly but strongly affected the range of $\mu*$ for which solutions could be obtained. The graph of the order-parameter variation with depth for all the cases is shown in figure 30. Note that, according to the model, the material is not a pure fluid ($p > 0$) at the free surface ($y = 0$).

The values of the parameter $\mu*$ correlate well with the effective friction coefficient μ_i, also given in table 4. Thus $\mu*$ depends on the frictional characteristics of the material as may be expected. The viscosity is nearly constant for different particle sizes and increases with rotational speed. The latter may be expected given the increase in the granular temperature with rotational speed.

Finally, we compare the experimental results obtained with the rheological model of Pouliquen and coworkers, (1.2). A direct comparison is possible in this case since μ and I can be estimated from the experimental data. Figure 31(*a*) shows the variation in the local coefficient of friction μ with the scaled shear rate I for the different data sets. The data sets are truncated and only the points in the dense flow region below the shear-rate maximum are shown. The data for the lower rotational speeds are all clustered toegther while the values of μ for the higher rotational speeds are

https://doi.org/10.1017/S002211200600320X Published online by Cambridge University Press

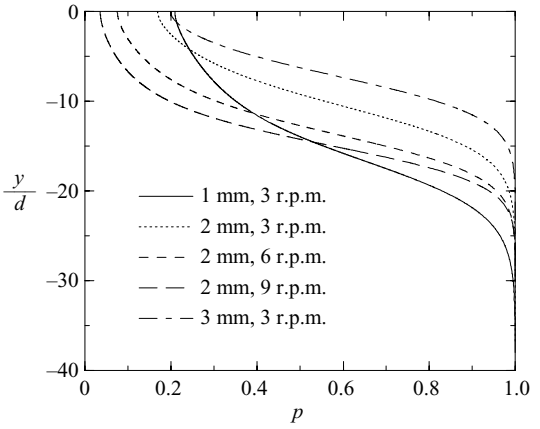


FIGURE 30. Variation in the order paramter p with depth in the flowing layer corresponding to the cases described in table 4.

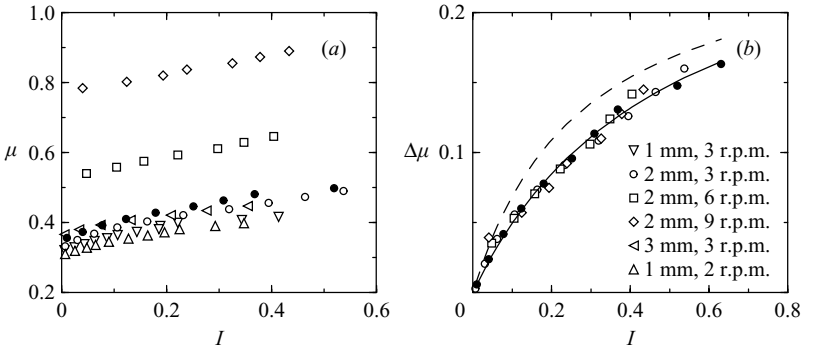


FIGURE 31. (*a*) Variation in the effective friction coefficient μ with scaled shear rate I for different particle sizes and cylinder rotational speeds, as indicated in the legend. The solid symbols correspond to 2 mm brass balls and a rotational speed of 3 r.p.m. (*b*) The increase in the coefficient of friction $\Delta\mu$ with scaled shear rate I for 2 mm particles. The solid line is a fit of (1.2) and the dashed line gives predictions of the same equation but using the parameters obtained by Jop *et al.* (2005).

significantly higher. This follows from the higher values of μ_i for the higher-r.p.m. data, seen in figure 13. We take μ_s to be the value of $\mu(I)$ extrapolated to $I = 0$. The range of μ_s for the low-r.p.m. data corresponds to angles ranging from 17 to 20 deg., which reflects the error in the estimation of μ. The values are in reasonable agreement with the results of Jop *et al.* (2005). Figure 31(*b*) shows the variation in $\Delta\mu = (\mu - \mu_s)$ with the scaled shear rate I for 2 mm particles and for different cyinder rotational speeds (3, 6 and 9 r.p.m.). The collapse of the data is reasonable, and the solid line is a fit to all the sets combined. The fit yields $\Delta\mu = \mu_2 - \mu_s = 0.29$ and $I_0 = 0.49$. The values reported by Jop *et al.* (2005) are $\Delta\mu = 0.261$ and $I_0 = 0.279$, and a plot of the model using these values is shown in figure 31(*b*) (dashed line). The difference between the two is not very large considering the different materials used here. Fits of the model gave slightly different model parameter values for 1 mm particles ($\Delta\mu = 0.18$, $I_0 = 0.48$) and 3 mm particles ($\Delta\mu = 0.20$, $I_0 = 0.43$), but only one set of data was available for fitting in each case.

https://doi.org/10.1017/S002211200600320X Published online by Cambridge University Press

4. Conclusions

An experimental study of surface flow in quasi-two-dimensional rotating cylinders was carried out using streakline photography. Experiments were performed for a wide range of rotational speeds and particle sizes. The mean-velocity profiles are linear over most of the layer depth in all cases, with an exponential decay near the base of the flowing layer and a flattened region near the free surface. The r.m.s. velocities are nearly constant in a region near the free surface; then there is a linear decrease over part of the layer and an exponential decay into the bed. The assumption of a linear velocity profile is thus only an approximation to the flow, but it is useful for describing the flow in a macroscopic sense as given by (1.1). Further, the r.m.s. velocities show a distinct anisotropy, the component in the flow direction being larger by a factor of about 1.5 than that perpendicular to the flow direction. The number densities are nearly constant across the flowing layer with a sharp decrease near the free surface. The shear and the normal stresses increase linearly with the depth of the flowing layer initially, but the shear stress deviates from linearity due to wall friction. The streaming stresses are found to be significant in the region near the free surface. The experimental velocity profiles reported here are broadly similar to those in previous works; however, a wider range of system parameters has been explored in this work.

The experimental data was analysed in several ways. A simple scaling is found to work very well. The mean velocity profiles for different cases scaled using the shear rate from Orpe & Khakhar (2001) and the particle diameter collapse to a single curve. A similar scaling works well for the r.m.s. velocity except for the region near the free surface. The shear rate obtained from a least-squares fit of the linear portion of the mean velocity profile is reasonably predicted by the model shear rate (1.1) but with a different value for the empirical constant c. For the model to be more useful, wall effects need to be factored into the model parameters c, β_s, β_m. The mean-velocity and r.m.s.-velocity profiles near the base of the layer are well described by an exponential function of the form $\exp(-y/\lambda)$, and the characteristic decay length λ is proportional to the particle diameter d in both cases, with $\lambda \approx 1.1d$ for the mean velocity and $\lambda \approx 1.7d$ for the r.m.s. velocity. Thus the r.m.s. velocity decays more slowly than the mean velocity.

The shear-rate profile obtained by numerically differentiating the mean-velocity profile data indicates that the shear-rate is not constant anywhere in the layer but increases to a maximum and then decreases to zero with depth in the layer. A transition in the r.m.s. profile occurs at the same depth as the shear-rate maximum: above the transition depth the r.m.s. velocity is nearly constant whereas below the transition depth it decreases with depth. Evidence of a transition is also seen in the variation of the velocity distributions with depth: above the transition point the distributions are Gaussian and below the transition point the velocity distributions gradually approach a Poisson distribution.

The rheology of the flow is characterised in terms of the variation in the apparent viscosity with the r.m.s. velocity. The curves indicate a relatively sharp transition at the shear-rate maximum, and in the region below this point the apparent viscosity varies as $\eta \sim u^{-1.5}$. The transition observed in the measurements appears to be a percolation type of transition, in which there is an increasing fraction of particles below the transition depth which are confined due to the formation of a network of particles in extended contact with each other. From the viewpoint of rheology, the flow comprises two layers, an upper low-viscosity layer with a nearly constant r.m.s. velocity and a lower layer of increasing viscosity with a decreasing r.m.s. velocity.

https://doi.org/10.1017/S002211200600320X Published online by Cambridge University Press

The thickness of the upper layer depends on the local flow rate but is independent of the particle diameter. In contrast, the lower layer thickness depends on the particle diameter but is independent of the flow rate. Thus after establishment of the lower layer any further increase in the local flow rate has the result that material passes through the upper layer. The rheological characteristics of the two layers are different.

The predictions of both models for the mean velocity match the experimental velocity profiles reasonably well. The model of Bonamy & Mills (2003) requires only two parameters, the shear rate, which can be independently obtained, and the characteristic length, which is found to be related in a simple way to the particle diameter ($\lambda = 4d$). This model, however, does not describe the low-density region near the free surface. The model of Aranson & Tsimring (2002) describes the entire velocity profile; however, experimental methods for independently estimating the parameter values need to be devised. A comparison of the predictions of the rheological model proposed by Pouliquen (Jop *et al.* 2005) with the experimental data also shows reasonable agreement when the increase in friction coeffcient with shear rate is considered. However, the coefficient of friction is found to be significantly higher at high local flow rates (corresponding to high rotational speeds), which is not in agreement with the model. The models considered show promise for prediction of the mean-velocity profile and the effective friction coefficient. More detailed rheological models are required for predicting r.m.s. velocities and velocity distributions which are important for transport.

The results presented in this paper give a reasonably detailed picture of the rheology of surface granular flows in quasi-two-dimensional systems. Although the results may be expected to be valid in qualitative terms for three-dimensional systems, wall effects cause significant quantitative differences. The walls impose two effects: one is side-wall friction, which is accounted for approximately in this work, and the second is ordering by the steric effects of the side walls. The measurements of Courrech-DuPont *et al.* (2005) indicate that wall friction reduces the velocity at the side wall by 20 %–30 % compared to that at the middle of the gap. Our preliminary results indicate that the effects of ordering may be larger: the mean velocity in long cylinders is about half that for a comparable quasi-two-dimensional system. Thus the ordering appears to reduce the effective viscosity of the system. Modelling such wall effects remains a challenge.

We are grateful for discussions with J. T. Jenkins, O. Pouliquen and I. Aranson. The computer program for the calculations in figures 29 and 30 was provided by I. Aranson, and we are grateful for his help. This paper was written while one of us (D. V. K.) was visiting Institut Henri Poincaré and the financial support of CNRS during the stay is gratefully acknowledged.

REFERENCES

Andreotti, B., Claudin, P. & Douady, S. 2002*a* Selection of dune shapes and velocities part 1: Dynamics of sand wind and barchans. *Eur. Phys. J.* B **28**, 312–339.

Andreotti, B., Claudin, P. & Douady, S. 2002*b* Selection of dune shapes and velocities part 2: A two-dimensional modelling. *Eur. Phys. J.* B **28**, 341–352.

Aranson, I. S. & Tsimring, L. S. 2002 Continuum theory of partially fluidized granular flows. *Phys. Rev.* E **65**, 061303.

Azanza, E., Chevoir, F. & Moucheront, P. 1999 Experimental study of collisional granular flows down an inclined plane. *J. Fluid Mech.* **400**, 199–227.

https://doi.org/10.1017/S002211200600320X Published online by Cambridge University Press

Bocquet, L., Losert, W., Schalk, D., Lubensky, T. C. & Gollub, J. P. 2001 Granular shear flow dynamics and forces: Experiment and continuum theory. *Phys. Rev.* E **65**, 011307.

Bonamy, D., Daviaud, F. & Laurent, L. 2002*a* Experimental study of granular surface flows via a fast camera: A continuous description. *Phys. Fluids* **14**, 1666–1673.

Bonamy, D., Daviaud, F., Laurent, L., Bonetti, M. & Bouchaud, J. P. 2002*b* Multiscale clustering in granular surface flows. *Phys. Rev. Lett.* **89**, 034301.

Bonamy, D., Faucherand, B., Planelle, M., Daviaud, F. & Laurent, L. 2001 Granular surface flows in rotating drum: experiments and continuous description. In *Powders and Grains* (ed. Y. Kishino), pp. 463–466. Swets and Zeitlinger, Lisse.

Bonamy, D. & Mills, D. 2003 Diphasic non-local model for granular surface flows. *Europhys. Lett.* **63**, 42–48.

Bouchaud, J. P., Cates, M. E., Ravi Prakash, J. & Edwards, S. F. 1994 A model for the dynamics of sandpile surface. *J. Phys. Paris* I **4**, 1383–1409.

Bounhoure, C., Brunet, Y. & Merlen, A. 2002 Hydrodynamic study of sedimantation flows and avalanches. *Powder Technol.* **125**, 306–312.

Boutreux, T. & de Gennes, P. G. 1996 Surface flows of granular mixtures: I. general principles and minimal model. *J. Phys. Paris* I **6**, 1295–1304.

Boutreux, T., Raphaël, E. & de Gennes, P. G. 1998 Surface flows of granular materials: A modified picture for thick avalanches. *Phys. Rev.* E **58**, 4692–4700.

Campbell, C. S. 1990 Rapid granular flows. *Annu. Rev. Fluid Mech.* **22**, 57–92.

Courrech-DuPont, S., Fischer, R., Gondret, P., Perrin, B. & Rabaud, M. 2005 Instantaneous velocity profiles during granular avalanches. *Phys. Rev. Lett.* **94**, 048003.

DaCruz, F., Emam, S., Prochnow, M., Roux, J.-N. & Chevoir, F. 2005 Rheophysics of dense granular materials: Discrete simulation of planar shear flows. *Phys. Rev.* E **72**, 021309.

Douady, S., Andreotti, B. & Daerr, A. 1999 On granular surface equations. *Eur. Phys. J.* B **11**, 131–142.

Hill, K. M., Gioia, G. & Tota, V. V. 2003 Structure and kinematics in dense free-surface flow. *Phys. Rev. Lett.* **91**, 064302.

Hutter, K. 1997 Snow and glacier rheology. *Appl. Rheol.* **7**, 266–276.

Hutter, K., Koch, T. & Savage, S. 1995 The dynamics of avalanches of granular materials from initiation to runout. part ii. experiments. *Acta Mech.* **109**, 127–143.

Jain, N., Ottino, J. M. & Lueptow, R. M. 2002 An experimental study of the flowing granular layer in a rotating tumbler. *Phys. Fluids* **14**, 572–582.

Jain, N., Ottino, J. M. & Lueptow, R. M. 2004 Effect of interstitial fluid on a granular flowing layer. *J. Fluid Mech.* **508**, 23–44.

Jop, P., Forterre, Y. & Pouliquen, O. 2005 Crucial role of side walls for granular surface flows: consequences for the rheology. *J. Fluid Mech.* **541**, 167–192.

Josserand, C., Lagree, P. Y. & Lhuillier, D. 2004 Stationary shear flows of dense granular materials: a tentative continuum modelling. *Eur. Phys. J.* E **14**, 127–135.

Khakhar, D. V., McCarthy, J. J., Shinbrot, T. & Ottino, J. M. 1997 Transverse flow and mixing of granular materials in a rotating cylinder. *Phys. Fluids* **9**, 31–43.

Khakhar, D. V., Orpe, A. V., Andresén, P. & Ottino, J. M. 2001*a* Surface flows of granular materials: model and experiments in heap formation. *J. Fluid Mech.* **441**, 255–264.

Khakhar, D. V., Orpe, A. V. & Hajra, S. K. 2005 Models for granular flow: Comparisons to experimental measurements. In *Powders and Grains 2005* (ed. Y. Garcia-Rojo, H. J. Hermann & S. McNamara), pp. 785–793. Balkema.

Khakhar, D. V., Orpe, A. V. & Ottino, J. M. 2001*b* Surface granular flows: Two related examples. *Adv. Complex Systems* **4**, 407–417.

Komatsu, T. S., Inagaki, S., Nakagawa, N. & Nasuno, S. 2001 Creep motion in a granular pile exhibiting steady surface flow. *Phys. Rev. Lett.* **86**, 1757–1760.

Longo, S. & Lamberti, A. 2002 Grain shear flow in rotating drum. *Exps. Fluids* **32**, 313–325.

Makse, H. A. 1999 Continuous avalanche segregation of granular mixtures in thin rotating drums. *Phys. Rev. Lett.* **83**, 3186–3189.

Mehta, A., ed. 1994 *Granular Matter: An Interdisciplinary Approach*. Springer.

MiDi, G. D. R. 2004 On dense granular flows. *Eur. Phys. J.* E **14**, 341–365.

Mills, P., Loggia, D. & Tixier, M. 1999 Model for a stationary dense granular flow along an inclined wall. *Europhys. Lett.* **45** (6), 733–738.

https://doi.org/10.1017/S002211200600320X Published online by Cambridge University Press

Mohan, L. S., Nott, P. & Rao, K. K. 1997 Fully developed flow of coarse granular materials through a vertial channel. *Chem. Engng Sci.* **52**, 913–933.

Mohan, L. S., Nott, P. & Rao, K. K. 2002 A frictional cosserat model for the slow shearing of granular materials. *J. Fluid Mech.* **457**, 377–409.

Mueth, D. M. 2003 Measurement of particles dynamics in slow, dense granular couette flow. *Phys. Rev.* E **67**, 011304.

Mueth, D. M., Debregeas, G. F., Karczmar, G. S., Eng, P. J., Nagel, S. R. & Jaeger, H. M. 2000 Signatures of granular microstructure in dense granular flows. *Nature* **406**, 385–388.

Nakagawa, M., Altobelli, S. A., Caprihan, A., Fukushima, E. & Jeong, E. K. 1993 Non-invasive measurements of granular flows by resonance imaging. *Exps. Fluids* **16**, 54–60.

Nedderman, R. M. 1992 *Statics and Kinematics of Granular Materials*. Cambridge University Press.

Orpe, A. V. & Khakhar, D. V. 2001 Scaling relations for granular flow in quasi-two-dimensional rotating cylinders. *Phys. Rev.* E **64**, 031302.

Orpe, A. V. & Khakhar, D. V. 2004 Solid-fluid transition in a granular shear flow. *Phys. Rev. Lett.* **93**, 068001.

Peray, K. 1986 *The Rotary Cement Kiln*. Chemical Publishing Company.

Perry, R. H. & Green, D. W. 1997 *Perry's Chemical Engineers' Handbook*, 7th Edn. McGraw-Hill.

Pouliquen, O., Forterre, Y. & Le Dizes, S. 2001 Slow dense granular flows as a self-induced process. *Adv. Comp. Sys* **4** (4), 441–450.

Press, W. H., Teukolsky, S. A., Vellerling, W. T. & Flannery, B. P. 1994 *Numerical Recipes in Fortran: The Art of Scientific Computing*, 2nd Edn., chap. 10. Cambridge University Press.

Quartier, L., Andreotti, B., Douady, S. & Daerr, A. 2000 Dynamics of a grain on a sandpile model. *Phys. Rev.* E **62**, 8299–8307.

Rajchenbach, J. 2003 Dense, rapid flows of inelastic grains under gravity. *Phys. Rev. Lett.* **90** (14), 144302.

Rajchenbach, J., Clement, E. & Duran, J. 1995 Experiments in model granular media : A study of gravity flows. In *Fractal Aspects of Materials* (F. Family, P. Meakin, B. Sapoval & R. Wool), vol. 327, pp. 525–528. Mat. Res. Soc. Symposium, Pittsburgh.

Renouf, M., Bonamy, D., Dubois, F. & Alart, P. 2005 Numerical simulation of two-dimensional steady granular flows in rotating drum: On surface flow rheology. *Phys. Fluids* **24**, 103303.

Savage, S. B. 1998 Analyses of slow high-concentration flows of granular materials. *J. Fluid Mech.* **377**, 1–26.

Taberlet, N., Richard, P., Valance, A., Losert, W., Pasini, J. M., Jenkins, J. T. & Delannay, R. 2003 Superstable granular heap in a thin channel. *Phys. Rev. Lett.* **91**, 264301.

Volfson, D., Tsimring, L. S. & Aranson, I. S. 2003 Partially fluidized shear granular flows: Continuum theory and molecular dynamics simulations. *Phys. Rev.* E **68**, 021301.

Wang, Z. & Zheng, X. 2004 Theoretical prediction of creep flux in aeolian sand transport. *Powder Technol.* **139**.

Zanuttigh, B. & Lamberti, A. 2002 Granular flow in equilibrium with the bottom: Experimental analysis and theoretical predictions. *Nonlinear Proc. Geophys.* **9**, 207–220.

https://doi.org/10.1017/S002211200600320X Published online by Cambridge University Press